The Astronomical Journal, 169:18 (26pp), 2025 January https://doi.org/10.3847/1538-3881/ad888a

CO Isotopologue-derived Molecular Gas Conditions and CO-to-H_2 Conversion Factors in M51

Jakob den Brok[1], María J. Jiménez-Donaire[2,3], Adam Leroy[4], Eva Schinnerer[5], Frank Bigiel[6], Jérôme Pety[7,8], Glen Petitpas[9], Antonio Usero[2], Yu-Hsuan Teng[10,11], Pedro Humire[12], Eric W. Koch[1], Erik Rosolowsky[13], Karin Sandstrom[11], Daizhong Liu[14], Qizhou Zhang[1], Sophia Stuber[5], Mélanie Chevance[15,16], Daniel A. Dale[17], Cosima Eibensteiner[18,25], Ina Galić[6,19], Simon C. O. Glover[15], Hsi-An Pan[20], Miguel Querejeta[2], Rowan J. Smith[21], Thomas G. Williams[22], David J. Wilner[1], and Valencia Zhang[1,23]

[1] Center for Astrophysics |Harvard & Smithsonian, 60 Garden Street, 02138 Cambridge, MA, USA
[2] Observatorio Astronómico Nacional (IGN), C/ Alfonso XII, 3, E-28014 Madrid, Spain
[3] Centro de Desarrollos Tecnológicos, Observatorio de Yebes (IGN), 19141 Yebes, Guadalajara, Spain
[4] Department of Astronomy, The Ohio State University, 140 West 18th Avenue, Columbus, OH 43210, USA
[5] Max Planck Institute for Astronomy, Königstuhl 17, 69117 Heidelberg, Germany
[6] Argelander-Institut für Astronomie, Universität Bonn, Auf dem Hügel 71, 53121 Bonn, Germany
[7] IRAM, 300 rue de la Piscine, F-38406 Saint Martin d'Hères, France
[8] Sorbonne Université, Observatoire de Paris, Université PSL, École normale supérieure, CNRS, LERMA, F-75005, Paris, France
[9] Massachusetts Institute of Technology, 77 Massachusetts Avenue, Cambridge, MA 02139, USA
[10] Department of Physics, University of California San Diego, 9500 Gilman Drive, La Jolla, CA 92093, USA
[11] Department of Astronomy & Astrophysics, University of California San Diego, 9500 Gilman Drive, La Jolla, CA 92093, USA
[12] Departamento de Astronomia, Instituto de Astronomia, Geofísica e Ciências Atmosféricas da USP, Cidade Universitária, 05508-900 São Paulo, SP, Brazil
[13] 4-183 CCIS, University of Alberta, Edmonton, Alberta, T6G 2E1, Canada
[14] Purple Mountain Observatory, Chinese Academy of Sciences, 10 Yuanhua Road, Nanjing 210023, People's Republic of China
[15] Institüt für Theoretische Astrophysik, Zentrum für Astronomie der Universität Heidelberg, Albert-Ueberle-Strasse 2, 69120 Heidelberg, Germany
[16] Cosmic Origins Of Life (COOL) Research DAO, Germany[24]
[17] Department of Physics and Astronomy, University of Wyoming, Laramie, WY 82071, USA
[18] NRAO, 520 Edgemont Road, Charlottesville, VA 22903, USA
[19] Max Planck Institute for Radio Astronomy, Auf dem Hügel 69, 53121 Bonn, Germany
[20] Department of Physics, Tamkang University, No.151, Yingzhuan Road, Tamsui District, New Taipei City 251301, Taiwan
[21] SUPA, School of Physics and Astronomy, University of St Andrews, North Haugh, St Andrews, KY16 9SS, UK
[22] Sub-department of Astrophysics, Department of Physics, University of Oxford, Keble Road, Oxford OX1 3RH, UK
[23] Phillips Academy, Andover, MA 01810, USA
Received 2024 July 26; revised 2024 October 15; accepted 2024 October 16; published 2024 December 10

Abstract

Over the past decade, several millimeter interferometer programs have mapped the nearby star-forming galaxy M51 at a spatial resolution of $\leqslant$170 pc. This study combines observations from three major programs: the PdBI Arcsecond Whirlpool Survey, the SMA M51 large program, and the Surveying the Whirlpool at Arcseconds with NOEMA. The data set includes the (1–0) and (2–1) rotational transitions of ^{12}CO, ^{13}CO, and C^{18}O isotopologues. The observations cover the $r < 3$ kpc region, including the center and part of the disk, thereby ensuring strong detections of the weaker ^{13}CO and C^{18}O lines. All observations are convolved in this analysis to an angular resolution of 4″, corresponding to a physical scale of 170 pc. We investigate empirical line ratio relations and quantitatively evaluate molecular gas conditions such as temperature, density, and the CO-to-H_2 conversion factor (α_{CO}). We employ two approaches to study the molecular gas conditions: (i) assuming local thermodynamic equilibrium (LTE) to analytically determine the CO column density and α_{CO}, and (ii) using non-LTE modeling with RADEX to fit physical conditions to observed CO isotopologue intensities. We find that the α_{CO} values in the center and along the inner spiral arm are ∼0.5 dex (LTE) and 0.1 dex (non-LTE) below the Milky Way inner disk value. The average non-LTE α_{CO} is $2.4 \pm 0.5\ M_\odot\ \mathrm{pc}^{-2}\ (\mathrm{K\ km\ s}^{-1})^{-1}$. While both methods show dispersion due to underlying assumptions, the scatter is larger for LTE-derived values. This study underscores the necessity for robust CO line modeling to accurately constrain the molecular interstellar medium's physical and chemical conditions in nearby galaxies.

Unified Astronomy Thesaurus concepts: Spiral galaxies (1560); Giant molecular clouds (653); Radio interferometry (1346); Radio spectroscopy (1359); Millimeter-wave spectroscopy (2252)

Materials only available in the online version of record: machine-readable table

1. Introduction

Rotational transitions of CO isotopologues remain one of the most accessible ways to trace the distribution, dynamics, and conditions of the bulk molecular gas in extragalactic studies of the nearby Universe. The molecular gas forms the reservoir for star formation, which occurs primarily within cold, dense giant molecular clouds (GMCs) that are distributed throughout the

[24] coolresearch.io
[25] Jansky Fellow of the National Radio Astronomy Observatory.

galaxy, forming part of the interstellar medium (ISM). The low-J transitional lines of ^{12}CO, the most abundant isotopologue, can be used to trace the general distribution and kinematics of galaxies, but they remain optically thick over most parts of the galaxy. In contrast, due to significantly lower abundances, other CO isotopologues remain optically thin, and their emission is generally an order of magnitude, or more, fainter than bright ^{12}CO line. After ^{12}CO, the next most abundant isotopologues are ^{13}CO and C^{18}O (T. L. Wilson & R. Rood 1994; C. Henkel et al. 2014). As a result, extragalactic studies have focused on low-J emission of these two CO isotopologue species, which make it possible to trace the entire column of CO-emitting molecular gas (e.g., T. A. D. Paglione et al. 2001; H.-A. Pan et al. 2015; M. J. Jiménez-Donaire et al. 2017; T. Brown & C. D. Wilson 2019; F. P. Israel 2020). By assuming optically thin emission for ^{13}CO and C^{18}O and comparing their intensities with the optically thick ^{12}CO lines, we can obtain constraints on the optical depth of the ^{13}CO or C^{18}O lines and relate them to variations in the molecular gas column densities (e.g., J. S. Young & N. Scoville 1982; J. E. Pineda et al. 2008; D. Cormier et al. 2018). Moreover, using multiple rotational-J emission lines for several CO isotopologue lines, it is possible to use radiative transfer models to infer the molecular gas conditions, such as temperature, density, and opacity (e.g., P. F. Goldsmith et al. 2008; F. P. Israel 2020; Y.-H. Teng et al. 2022, 2023; D. Liu et al. 2023). Consequently, CO isotopologue line ratios have become a strong diagnostic tool for evaluating the chemical (e.g., abundances) and physical (e.g., temperature, density) properties of molecular gas. A challenge, however, remains that without a sufficient number of rotational-J line observations, studies of line ratios are affected by degeneracies, as differences in relative abundance, beam filling factors, opacities, and changes in temperature and density will all affect the measured ratios.

Initially, our knowledge on the variation of the ^{13}CO and C^{18}O line emission—and subsequently their abundance ratio—across the ISM was limited to the Milky Way (e.g., W. D. Langer & A. A. Penzias 1990; T. L. Wilson & R. Rood 1994). In extragalactic studies, at first, the focus was on bright, actively star-forming systems where higher column densities and warmer gas made it possible to detect faint CO isotopologues (e.g., D. S. Meier & J. L. Turner 2004; F. Costagliola et al. 2011; R. Aladro et al. 2013). Such systems include (ultra)luminous infrared galaxies, starburst galaxies, or galaxy centers in general. More recently, studies on kiloparsec scales have provided us with insights into the variation of the various CO isotopologue ratios across normal (i.e., main-sequence) star-forming galaxies and their relation to global galactic properties (e.g., T. A. Davis 2014; M. J. Jiménez-Donaire et al. 2017; J. S. den Brok et al. 2022; Y. Cao et al. 2023). These studies report, for instance, an increasing ^{13}CO/C^{18}O intensity ratio with increasing galactocentric radius and a decrease with increasing star formation rate (SFR) surface density (M. J. Jiménez-Donaire et al. 2017), or increasing ^{12}CO/^{13}CO intensity ratios with the SFR surface density (T. A. Davis 2014; Y. Cao et al. 2023). From these studies alone, it remains unclear to what degree these observed ratio variations are the result of changes in the opacity due to different densities of molecular gas or changes in the relative abundances due to physical or chemical processes that affect the amount of the CO isotopologue species. Studies that focus on numerous rotational-J transitions to break the aforementioned degeneracy to some degree are still limited mainly to the bright centers of nearby star-forming galaxies (e.g., F. P. Israel 2020; Y.-H. Teng et al. 2022, 2023).

Given a set of rotational-J CO (isotopologue) lines, a common approach in the literature is to assume local thermodynamic equilibrium (LTE; e.g., T. L. Wilson et al. 2009), which makes it possible to solve the equations of radiative transfer analytically and infer the molecular gas conditions. This technique is generally (computationally) easy and fast to implement and only requires the detection of two emission lines (optically thick ^{12}CO and optically thin ^{13}CO) to constrain the excitation temperature, the opacity, and the CO column density. Therefore, this is often the preferred approach for extragalactic studies of nearby galaxies (e.g., D. Rigopoulou et al. 1996; G. Dahmen et al. 1998; T. A. D. Paglione et al. 2001; J. Braine et al. 2010; T. A. Davis 2014; D. Cormier et al. 2018; K. Morokuma-Matsui et al. 2020; Y. Cao et al. 2023), where multi-CO line surveys are challenging to achieve due to the required sensitivity of the observations. However, the underlying assumption that the level populations are following thermal equilibrium is often not accurate in the molecular ISM (e.g., Y. L. Shirley 2015). Therefore, non-LTE software tools have been developed, which can solve the radiative transfer equations numerically and do not require the level populations to be in thermal equilibrium. Such an implementation that models line intensities for a specified set of physical conditions is `RADEX` (F. F. S. van der Tak et al. 2007). To obtain robust constraints, multiple CO lines have to be observed to limit the number of free parameters. Therefore, non-LTE approaches are not only computationally, but also observationally more expensive. Consequently, extragalactic studies employing the non-LTE approach are generally limited to focusing on bright galaxy centers (e.g., F. P. Israel 2020; Y.-H. Teng et al. 2022, 2023) or brighter starburst or merging galaxies (e.g., D. Salak et al. 2014; H. He et al. 2024). With our data set of M51 at hand, which contains several CO isotopologue lines, we can compare the use of an LTE and non-LTE approach simultaneously to contrast the two methods and constrain key parameters, such as CO column density and the CO-to-H_2 conversion factor in the context of regular galaxy conditions beyond the center or starburst regime. So far, these LTE and non-LTE multi-line modeling efforts for extragalactic observations often rely on simplistic one- or two-zone models to describe the molecular gas distribution due to limitations imposed by the number of detected lines and the angular resolution. A one-zone description is, however, generally only a poor representation of the actual underlying (sub-beam) gas distribution. For instance, turbulent theories, supported by Milky Way observations that resolve individual clouds (e.g., P. F. Goldsmith et al. 2008; J. Kainulainen et al. 2009; M. Tafalla et al. 2023), predict a range of densities that follow a lognormal distribution within each cloud (P. Padoan & Å. Nordlund 2002). A. K. Leroy et al. (2017a) investigated how the sub-beam density distribution affects the beam-averaged emissivity in the context of extragalactic observations. Their findings suggest that the beam-averaged emissivity of dense gas tracers (e.g., HCN, HCO$^+$) is highly sensitive to variations in sub-beam density distributions, whereas the low-J CO line emission is relatively insensitive to these variations. Therefore, while a single- or two-component CO line modeling approach should be interpreted with care, it can still be viable

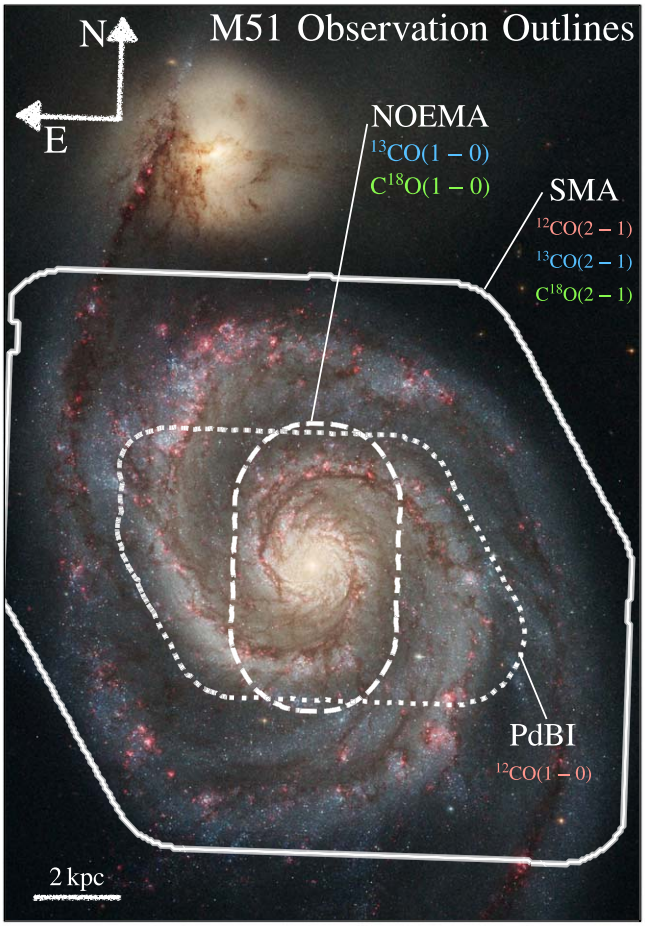

Figure 1. Spatial coverage of observations. In this study, we rely on Plateau de Bure Interferometer (PdBI), Northern Extended Millimeter Array (NOEMA), and Submillimeter Array (SMA) observations, each of which covered some extent of the disk of M51. The boxes indicate which lines were observed by each respective program. Background HST image credit: NASA, ESA, S. Beckwith (STScI), and The Hubble Heritage Team (STScI/AURA).

for capturing the bulk gas properties. This study focuses on the bright face-on nearby grand-design spiral galaxy M51 (NGC 5194). It is at a distance of $D \approx 8.6$ Mpc (K. B. W. McQuinn et al. 2016)—so an angular resolution of $4''$ translates to a physical resolution of $\sim$170 pc. The galaxy interacts tidally with a companion (see Figure 1). The disk is dominated by molecular gas (K. F. Schuster et al. 2007; A. K. Leroy et al. 2008), making it possible to also detect the fainter CO isotopologues across a large part of the star-forming disk of M51. The spiral arms are particularly prominent in observations across the electromagnetic spectrum. Also, the molecular gas is clearly distributed along these spiral arms (J. Koda et al. 2011; E. Schinnerer et al. 2013; J. Pety et al. 2013). In a previous IRAM 30 m large program study (CLAWS; J. S. den Brok et al. 2022, hereafter dB22), the CO isotopologue line emission of ^{12}CO, ^{13}CO, and C^{18}O across the disk at kiloparsec scales has been studied. Galaxy-wide, the various CO isotopologue line ratios investigated there show trends in agreement with selective nucleosynthesis and changes in optical depth as main drivers. Here, we follow up this study by investigating the same line ratios at higher physical resolution to obtain a more detailed view of the potential drivers of CO isotopologue line ratio variation.

This paper is structured as follows: We describe the various data sets used in Section 2. In Section 3, we present the main results of this study, including the line ratio trends across the central $r < 3$ kpc region of M51 and the variation in molecular gas properties derived from radiative transfer calculations. We discuss the interpretation of the results in Section 4. We conclude in Section 5.

2. Data and Observations

Here, we use observations of the (1–0) and (2–1) rotational transitions of ^{12}CO, ^{13}CO, and C^{18}O from two different millimeter interferometers. The outlines in Figure 1 illustrate the spatial extent of the different observations. We provide a summary of the CO isotopologue line observations in Table 1. We present all spectra in terms of the line-of-sight velocity, $v_{\rm LSR}$, relative to the local standard of rest.

2.1. Plateau de Bure Interferometer—^{12}CO(1–0)

The PdBI Arcsecond Whirlpool Survey (PAWS) observed the ^{12}CO(1–0) line emission at $1''$ ($\approx$40 pc) resolution across the center and a large part of the disk of M51 (E. Schinnerer et al. 2013). The precise field of view (FOV) of the observation is highlighted in Figure 1. The observations of the Plateau de Bure Interferometer (PdBI) have been short-spacing corrected using IRAM 30 m single-dish data. The data reduction is described in J. Pety et al. (2013).

2.2. Northern Extended Array—^{13}CO and C^{18}O(1–0)

The Surveying the Whirlpool at Arcseconds with NOEMA (SWAN) is an IRAM large program (LP003 PIs: E. Schinnerer, F. Bigiel; S. K. Stuber et al. 2023). Observations were carried out using the Northern Extended Millimeter Array (NOEMA) and IRAM 30 m single dish for short-spacing corrections. The observations targeted several molecular lines in the 3 mm line window within the central 5×7 kpc of M51 (see the outline in Figure 1). The spectral coverage of the program includes the 1–0 transitions of ^{13}CO and C^{18}O. The data have a native angular resolution of $\sim 2\farcs5$ ($\sim$ 100 pc). For details about the data calibration and reduction, we refer the reader to S. Stuber et al. (2024, in preparation).

2.3. Submillimeter Array—^{12}CO, ^{13}CO, and C^{18}O(2–1)

As part of a Submillimeter Array (SMA) Large Program (2016B-S035, PI: K. Sliwa), the molecular disk of M51 was observed in three configurations: subcompact (SUB), compact (COM), and extended (EXT). While the SUB configuration consists of 147 pointings, covering the entire molecular disk of M51, the observations in COM consist of 55 pointings covering the same footprint as the PAWS data. The SMA observations include the ^{12}CO(2–1), ^{13}CO(2–1), and C^{18}O(2–1) lines. For the subsequent analysis, we combine the observations in COM and SUB configurations, limiting the footprint to the overlapping FOV (which is equivalent to the PAWS FOV). Furthermore, the SMA observations have been short-spacing corrected using IRAM 30 m observations from the CLAWS large program (dB22). We document the details of the data reduction steps in Appendix A.

Table 1
Summary of the CO Isotopologue Line Observations Relevant in This Study

Line	$\nu_{\rm rest}$ (GHz)	Native Beam[a] ($''$)	⟨Sensitivity⟩[b] (mK)	Completeness[c] (%)	Telescope/Survey/Reference
$C^{18}O$(1–0)	109.782	2.5 × 2.2	14	32	NOEMA / SWAN
^{13}CO(1–0)	110.201	2.4 × 2.1	17	63	S. Stuber et al. (2024, in preparation); see also S. K. Stuber et al. (2023)
^{12}CO(1–0)	115.271	1.1 × 1.1	105	100	PdBI / PAWS / E. Schinnerer et al. (2013)
$C^{18}O$(2–1)	219.560	4.1 × 4.1	55	2	SMA / SMA-PAWS / this study; see Appendix A
^{13}CO(2–1)	220.399	4.1 × 4.1	70	14	
^{12}CO(2–1)	230.538	3.9 × 3.9	90	73	

Notes.
[a] The beam size of the original data. For the subsequent analysis, we convolve all cubes to a common beam size of $4''$.
[b] The median rms of the data convolved to $4''$, per 5 km s^{-1} channel width.
[c] Percentage of sight lines (i.e., spatial pixels) with respect to ^{12}CO(1–0) within the NOEMA field of view (FOV) that have significant detection (per definition, it is 100% for ^{12}CO(1–0)).

2.4. Ancillary Data Sets

In this study, we compare the distribution and derived properties of the molecular gas from the CO isotopologues to the distribution of the SFR across M51. For this purpose, we need comparable high angular resolution SFR tracers. Previous studies that investigated the connection between the molecular gas condition and star formation in M51 mainly relied on IR-based SFR tracers (e.g., A. K. Leroy et al. 2017b,dB22). However, these IR-based tracers are limited in angular resolution to $\geqslant 10''$.

In this study, we use 33 GHz extended Very Large Array (EVLA) observations of M51 (M. Querejeta et al. 2019) to trace the SFR. The angular resolution of this data is $\sim 3''$. The 33 GHz continuum, which mainly traces free–free emission, is empirically calibrated to a measure of SFR (E. J. Murphy et al. 2011). We use the SFR surface density map derived by M. Querejeta et al. (2019). For extensive details on the particular method to compute the SFR surface densities, we refer to M. Querejeta et al. (2019). In short, they estimated the thermal fraction (i.e., fraction from free–free emission) in individual 100 pc apertures by contrasting the 33 GHz emission to other radio bands (including the 1.4, 4.9, and 8.4 GHz bands). They report typical thermal fractions of 55%–75% in M51.[26] The free–free luminosity, $L^{T}_{33\,\rm GHz}$, can then be converted to an SFR estimate using the following empirical relation (E. J. Murphy et al. 2011):

$$\left(\frac{\rm SFR}{M_\odot\ \rm yr^{-1}}\right) = 1.5 \times 10^{-27} \cdot \left(\frac{T_e}{10^4\ \rm K}\right)^{-0.45} \cdot \left(\frac{L^{T}_{33\,\rm GHz}}{\rm erg\ s^{-1}\ Hz^{-1}}\right), \quad (1)$$

where T_e describes the electron temperature (following M. Querejeta et al. 2019, we assume $T_e = 6300$ K based on previous observations by K. V. Croxall et al. 2015). For the calculation, we use a thermal fraction of 75%.

We note that the VLA data has not been short-spacing-corrected. Therefore, given the uncertainty of the missing flux (see M. Querejeta et al. 2019 for details), we emphasize that the SFR measurements represent a lower limit. We stress, however, as the observations were carried out using the very compact configuration of the VLA interferometer (sensitive to spatial scales up to $44'' \approx 1.6$ kpc), flux filtering effects will be limited. This is further supported by E. J. Murphy et al. (2018), who found that the missing flux is not significant when comparing VLA and GBT single-dish observations.

2.5. Data Homogenization and Processing

For a proper analysis combining all of the CO isotopologue line observations from various observatories, we use the`PyStructure`[27] pipeline code (J. den Brok et al. 2024). This tool convolves all cubes to a common beam size and regrids them to a hexagonal grid with 5 km s^{-1} channel width. We convolve all cubes and maps to $4''$ resolution with a Gaussian kernel using the astropy`convolve` function. We resample each cube and map on a hexagonal grid of points, which are half-beam sized separated (i.e., $2''$). The grid spans the entire FOV of the ^{12}CO(1–0) observation. The particular steps are done using the`PyStructure` pipeline presented in dB22.

The CO isotopologue data cubes are processed in this framework to derive the moment-0 ("integrated intensity"), moment-1 ("weighted sight-line velocity"), and moment-2 ("line FWHM") maps.[28] The moment-0 is computed by integrating over a masked spectral range. The range we integrate over is sight-line dependent. For this computation, the same velocity range is used for each line. We use the highest-S/N line, ^{12}CO(1–0), to determine the spectral range where we expect emission by expanding the high-S/N > 4 mask into the low-S/N > 2 mask, such that only those connected voxels at S/N > 2 remain that are associated with an S/N > 4 peak. For the moment-1 and moment-2 calculations, we determine a stricter mask for each sight line and for each CO isotopologue line separately. This mask requires that at least three consecutive channels are significantly detected above 4σ of the rms. To estimate the error and uncertainty, we compute the standard deviation of the line-free part of the spectrum per sight line for each CO isotopologue. This yields the noise per 5 km s^{-1} channel width. We propagate the errors assuming independent channels to compute the noise for the different moment maps.

[26] This thermal fraction is lower compared to other galaxies, where fractions of ∼90% are reported (S. T. Linden et al. 2020). The low thermal fraction in M51 is likely related to the ongoing merger with its companion galaxy M51b and the fact that the AGN likely also contributes diffuse synchrotron emission

[27] https://github.com/jdenbrok/PyStructure/

[28] To convert the FWHM to a Gaussian line width equivalent, σ, we need to divide the former by the factor 2.355.

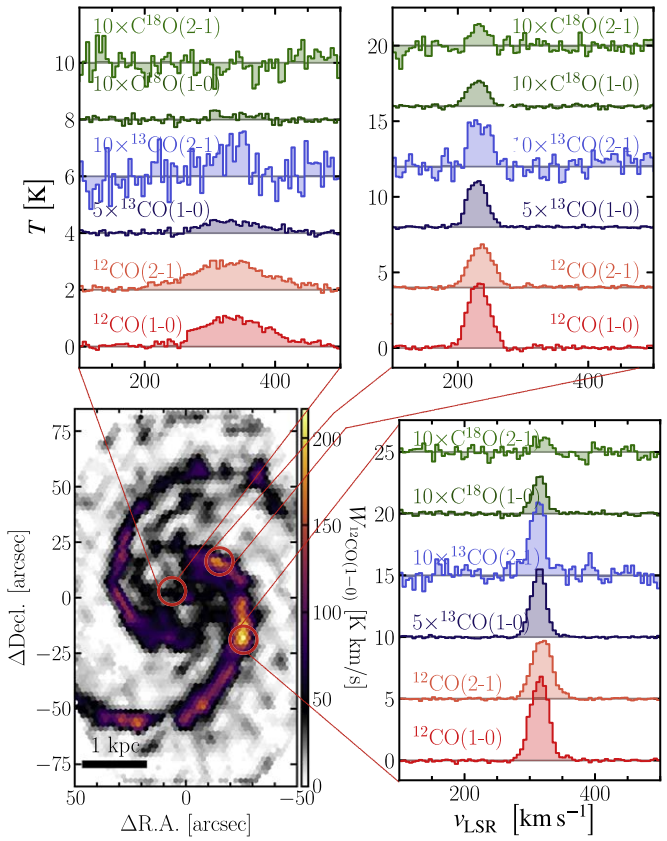

Figure 2. CO Isotopologue line detection. The bottom-left panel illustrates the ^{12}CO(1–0) moment-0 map in units of K km s^{-1}. The other three panels present the line emission spectra for three selected pointings in the galaxy. The spectra are each plotted with an incrementing offset, from the top-left to the bottom-right panel, of $\Delta T_{\rm mb}$ = 5 K, 2 K, and 4 K, respectively. We scale the ^{13}CO and C^{18}O spectra by a factor of 5 or 10 such that the line emission is visible when compared to the much brighter ^{12}CO line.

Figure 2 illustrates the resulting data set used in the subsequent analysis. The bottom panel shows the moment-0 map of ^{12}CO(1–0), convolved to 4″ and resampled on a hexagonal grid. We depict the spectral lines for three selected points within the central region of M51 where we expect significant emission from all six CO isotopologue lines.

2.5.1. Spectral Line Stacking

To improve the signal-to-noise and retrieve trends with key galactic parameters, we employ a spectral line stacking method, which is described in detail in A. Schruba et al. (2011), A. Caldú-Primo et al. (2013), M. J. Jiménez-Donaire et al. (2019), and L. Neumann et al. (2023). In short, spectral stacking consists of first velocity-normalizing the spectra (i.e., shifting the profiles such that any velocity offsets due to rotation and/or nonstreaming motions relative to the systemic velocity of the galaxy are removed), then binning these spectra by a respective quantity, and finally averaging the spectra per bin. This technique exploits the fact that the noise will not add coherently unlike any faint emission present in the data. For more details and an analysis of the performance of the method for interferometric data, we refer to L. Neumann et al. (2023).

We stack the data by galactocentric radius, SFR surface density, and FWHM of the ^{12}CO(1–0) emission line. For galactocentric radius, the stacking bins range from 0–3 kpc in steps of 300 pc bin-width. For SFR surface density, we use logarithmic bins. We use 10 bins ranging from $\log(\Sigma_{\rm SFR}/(M_\odot\ {\rm yr}^{-1}\,{\rm kpc}^{-2})) = -3$ to 0. For FWHM, we also use logarithmic bins ranging from 8–70 km s^{-1}.

2.5.2. CO Line Ratio Computation and Notation

We compute the integrated line intensity ratios (hereafter just "line ratio") by dividing the moment-0 maps. In our analysis, we refer to line ratios as significant if both lines are detected with a significance of $\geqslant 5\sigma$, which translates into a $\gtrsim 4\sigma$ ratio measurement. We note that the number of significant detections (and hence the spatial distribution) varies for each line ratio depending on the sensitivity and strength of the two lines. We illustrate the spatial extent for the significantly detected sight lines per line ratio in Appendix B. The $\geqslant 5\sigma$ threshold translates into a molecular gas point-source mass sensitivity[29] for ^{12}CO(1–0) of $\sim 1 \times 10^6\,M_\odot$. In this paper, we refer to the line ratios with the following notation. The superscript indicates which CO isotopologue(s) is(are) used. The subscript indicates information about the rotational-J transition. For instance, $R_{10}^{13/12}$ is the ^{13}CO/^{12}CO(1–0) integrated intensity ratio, and R_{21}^{12} indicates the ^{12}CO(2–1)/(1–0) ratio.[30] In case one of the two lines is not detected (i.e., S/N < 5), we compute a limit. If the line in the numerator is not detected, it will be an upper limit. In case the line in the denominator is not detected, we will compute a lower 5σ limit. The limit is computed using the measured spectral rms and assuming a line width of 20 km s^{-1}.

We note that the use of sigma-clipping introduces a bias toward CO-bright regions in M51, such as the central area and the onset of the spiral arms. This is particularly important for ratios involving the fainter ^{13}CO(2–1) and C^{18}O(2–1) lines, where both the reduced line strength and the lower sensitivity of the SMA observations limit the detectable signal. In contrast, when stacking, we incorporate all sight lines, regardless of detection significance, reducing the bias toward CO-bright regions. Consequently, stacking may result in different averages compared to a traditional median, as the inclusion of sight lines with nondetections potentially shifts the overall value. Therefore, we view the stacking results as being more robust (less biased) and hence focus, in particular for the derived line ratio trend analysis, on using stacking results.

3. Results

We first focus on the overall CO isotopologue line ratio trends across the central $r < 3$ kpc region of M51. For this purpose, we compute the azimuthally averaged and (galactocentric) radial trends. We also investigate the isotopologue ratio trends with the SFR surface density and the ^{12}CO(1–0) line FWHM. We then perform an LTE line modeling analysis based on the ^{12}CO excitation and the ^{12}CO/^{13}CO(1–0) ratios. Finally, we also present results from a non-LTE line modeling approach using RADEX.

3.1. General CO Isotopologue Line Ratio Trends

We first investigate the sight lines for which we have significantly detected line ratio values. Earlier studies found such radial trends based on resolved measurements of CO

[29] Assuming a line width of 15 km s^{-1} and a conversion factor of 2 $M_\odot$ pc^{-2}(K km s^{-1})$^{-1}$.

[30] The line ratio of two different rotational transitions is abbreviated by the subscript as "21":2 → 1/1 → 0. This is also evident if the superscript only contains one CO isotopologue.

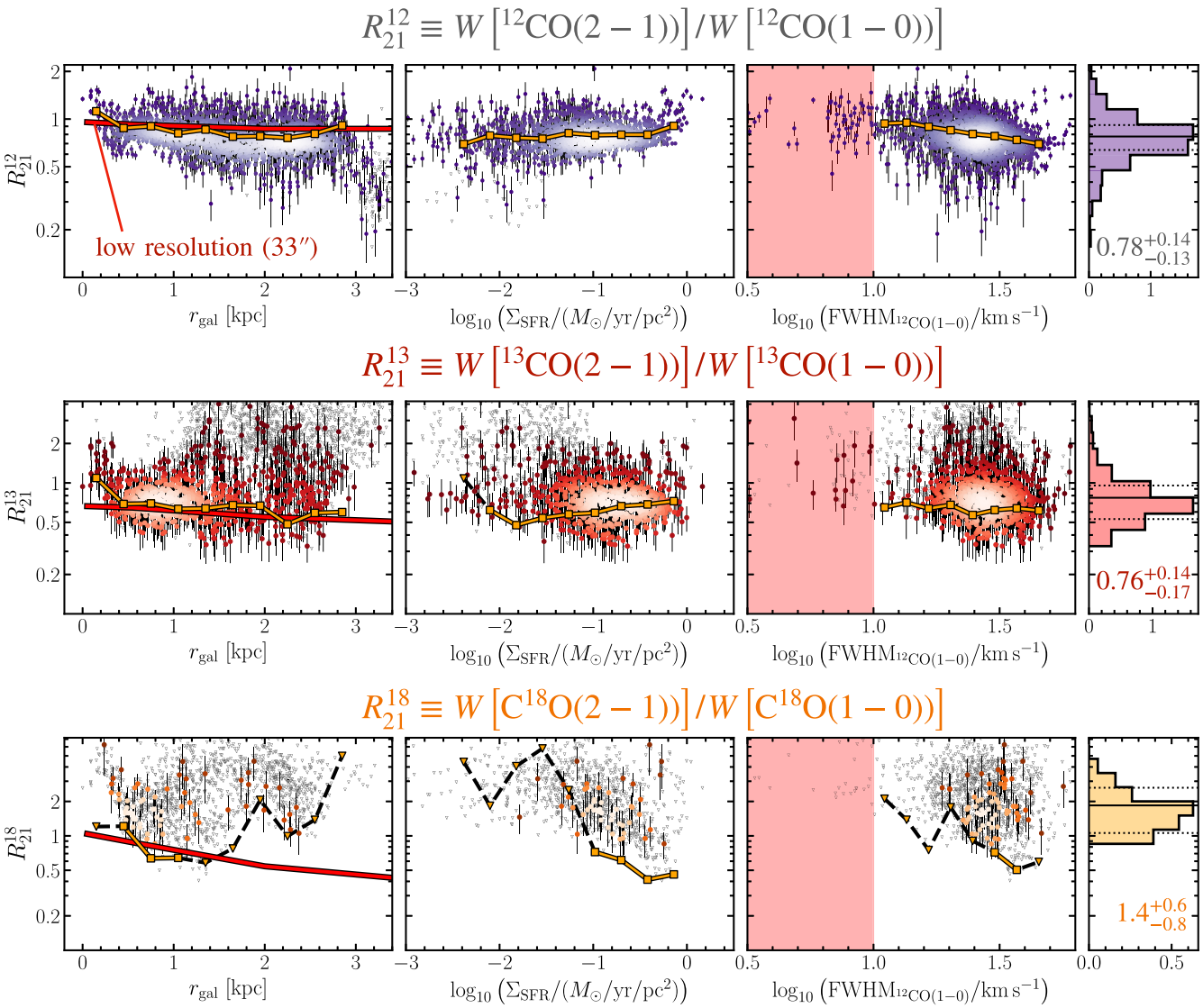

Figure 3. CO isotopologue ratio trends. These panels show the line ratio as a function of galactocentric radius (left panel), SFR surface density (middle panel), and FWHM of ^{12}CO(1–0) (right panel) panel. Only lines of sight within the NOEMA FOV are considered. We show the individual sight lines where both lines have S/N $\geqslant 5$ as colored points. The small black triangles indicate 5σ upper limits. In addition, the orange line depicts the stacked line ratio trend. We stack all points for which ^{12}CO(1–0) is significantly detected. The red line in the left panels is the radial trend obtained at low-angular resolution from (dB22). The red shaded region in the right panels indicates where the FWHM is below two times the channel width of our data (10 km s^{-1}). The histograms show the distribution of these significantly detected data points per line ratio. The black line represents the weighted average (weighted by the ^{12}CO(1–0) intensity), and the dotted lines represent the weighted 16th-to-84th percentile range.

isotopologues and C and O isotopes in the Milky Way (W. D. Langer & A. A. Penzias 1990; S. N. Milam et al. 2005; Y. T. Yan et al. 2023) and nearby galaxies (e.g., M. J. Jiménez-Donaire et al. 2017; D. Cormier et al. 2018; S. Martín et al. 2019). We compare these ratios to the SFR surface density, because it relates to and traces to some degree the molecular gas conditions. Particularly, we expect higher SFR surface density to correlate with hotter (heated by young stars) or denser (gas in the process of forming stars) gas (D. Narayanan & M. R. Krumholz 2014). Finally, we also contrast the line ratios to the ^{12}CO(1–0) line FWHM, which we expect to trace besides the larger-scale gas motions, and additionally, to some limited degree, the turbulence of the gas (P. L. Baker 1976; R. Shetty et al. 2011). We also expect that the turbulence of the gas has an impact on the optical depth of the CO emission (R. Shetty et al. 2011). The trends are shown in Figures 3 and 4 and relevant correlation coefficients are provided in Table 2. If not specifically stated, the trends refer to the stacked line ratio measurements.

3.1.1. R_{21}^{12} Ratio

R_{21}^{12} has been thoroughly studied at low (kiloparsec-scale) and high (cloud-scale) angular resolution across and within nearby galaxies (e.g., J. Koda et al. 2012; T. Brown et al. 2021; Y. Yajima et al. 2021; A. K. Leroy et al. 2022; J. S. den Brok et al. 2023a). Using our high angular resolution observations (see the top panel of Figure 3), we report a disk-wide, ^{12}CO(1–0) intensity weighted line ratio average and 16th-to-84th percentile range of $\langle R_{21}^{12}\rangle^{\mathrm{weight.}} = 0.78^{+0.14}_{-0.13}$. At 33″ angular resolution, the line ratio appears flat as a function of galactocentric radius within the central 3 kpc of the galaxy (see the red line in the left panel of Figure 3). At 4″ angular resolution, we observe a flat trend of R_{21}^{12} with an increase

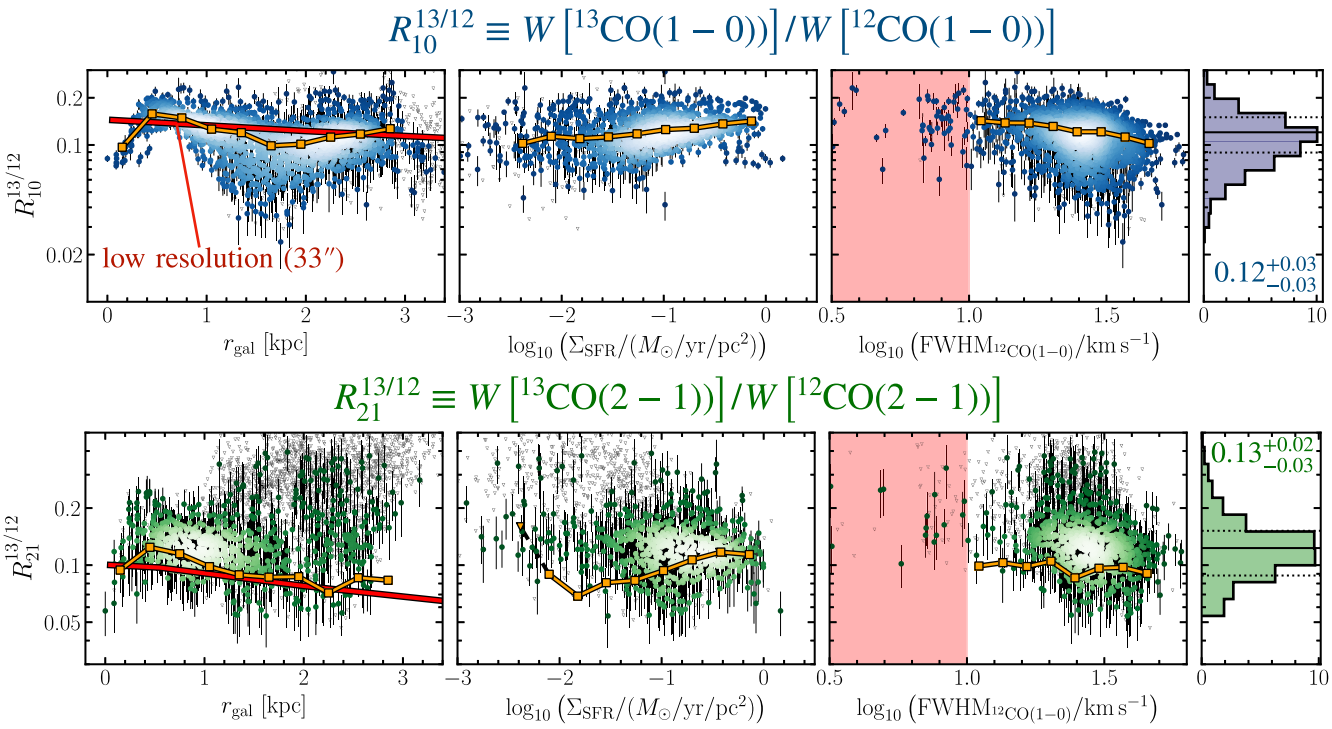

Figure 4. CO isotopologue ratio trends (continued). These panels have the same description as in Figure 3.

toward the central $r < 500$ pc radii. The individual sight lines show a sharp decrease from the center to 0.25 kpc from a value of ∼1.25 to ∼0.9, while R_{21}^{12} flattens at $r_{\mathrm{gal}} \geqslant 0.5$ kpc (the orange line).[31] The observed decrease at 3 kpc of individual sight lines is likely related to incomplete radial sampling.

We observe a slight positive correlation of R_{21}^{12} with SFR surface density. Fitting a linear regression to the stacked ratio trend in log-log space, we find a slope of $m = 0.08$. We note that this value is less steep (but within the expected range of scatter) than the slope of $m = 0.129$ reported by A. K. Leroy et al. (2022) across a sample of 90 nearby galaxies at kiloparsec scales and $m = 0.10 \pm 0.02$ measured by J. S. den Brok et al. (2023a) at ∼200 pc scale resolution in NGC 3627. Finally, we find a negative, statistically significant anticorrelation between the ^{12}CO(1–0) FWHM and R_{21}^{12}.

3.1.2. R_{21}^{13} Ratio

Due to their fainter emission compared to the ^{12}CO low-J transition, we have fewer significantly detected sight lines for which we can report a significant R_{21}^{13} ratio value. We report a ^{12}CO(1–0) weighted average and 16th-to-84th percentile range for the significantly detected sight lines of $\langle R_{21}^{13}\rangle^{\mathrm{weight.}} = 0.76^{+0.14}_{-0.17}$. The stacked trend is within the margin of scatter of the galaxy-wide average of $\langle R_{21}^{13}\rangle^{\mathrm{weight.}}_{\mathrm{lowres}} = 0.61^{+0.09}_{-0.08}$ noted by dB22 at 33″ resolution. Similar to R_{21}^{12}, we measure a mild decreasing trend of the line ratio with increasing galactocentric radius. From the stacked line ratio trend, we measure a decreasing slope of $m = -0.07$. From $r_{\mathrm{gal}} = 0.0$–0.5 kpc, the decrease is stronger with a negative slope of ~ -1.5. Also similar to R_{21}^{12}, we find an increasing trend with the SFR surface density. With $m = 0.065$ (p value of 0.03), the slope in log-log space is slightly more shallow than the R_{21}^{12} correlation in its value. Finally, R_{21}^{13} does not show a significant correlation with the FWHM of ^{12}CO(1–0). We measure $m \approx 0$ (p value of 0.79) in log-log space for the stacked trend. We cannot rule out that the lack of any correlation is driven by the low S/N of the ^{13}CO(2–1) line, which results in lower stacked intensities as we sum over a more significant fraction of noise.

3.1.3. R_{21}^{18} Ratio

For C^{18}O(2–1), we have the smallest number of significantly detected sight lines of only 65 sight lines where R_{21}^{18} has S/N ⩾ 5 (compared to 2485 sight lines for R_{21}^{12} and 298 sight lines for R_{21}^{13}; see percentage completeness in Table 1). For these significantly measured line ratios, we find a luminosity weighted average and 16th-to-84th percentile range of $\langle R_{21}^{18}\rangle^{\mathrm{weight.}} = 1.4^{+0.5}_{-0.6}$. We note that this is significant higher than the transition ratios of ^{12}CO and ^{13}CO we report here in this study. Furthermore, the CLAWS survey reported ratio at 33″ is also lower with $\langle R_{21}^{18}\rangle^{\mathrm{weight.}}_{\mathrm{lowres}} = 0.87^{+0.24}_{-0.15}$ (dB22), although in agreement within the scatter. In contrast, the stacked ratio is around 0.7, which is more comparable to the other CO line transition ratios. The reason for this high ratio measured for the individual sight line most likely is due to an observational bias. The C^{18}O(2–1) emission is only marginally detected across our map. Therefore, low R_{21}^{18} line ratio values, where the 2–1 emission tends to be fainter, are likely censored and not significantly detected. Only when stacking can we probe the full parameter space and measure lower R_{21}^{18}. Since only 2–3 stacked measurements are significant, we do not analyze or

[31] A note of caution when interpreting the stacked line ratio trends (see also explanation in Section 2.5.2): in the various panels, we show the individual sight lines as single data points. For the stacking, however, we also include sight lines where the line emission (apart from ^{12}CO(1–0)) is insignificant. If, for a given bin, the number of pixels without significant detection dominates, then the resulting line stack will have a lower intensity. In addition, since we use a logarithmic scaling for the y-axis, we can only show the positive nondetection. This explains why certain stacked trends fall below the distribution of significantly detected points in Figures 3 and 4.

Table 2
Summary of Line Ratio Results

Ratio	n_{det}[a]	Weighted Mean and Scatter[b]			Stacked Trends[c] (slope/intercept/p value)		
		Entire Map	Center	Disk	r_{gal}	Σ_{SFR}	FWHM$_{^{12}CO(1-0)}$
R_{21}^{12}	2485	$0.78^{+0.14}_{-0.13}$	$0.89^{+0.15}_{-0.15}$	$0.76^{+0.14}_{-0.13}$	−0.031/−0.022/0.092	0.08/−0.10/0.095	−0.24/0.25/6.2 × 10^{-6}
R_{21}^{13}	298	$0.76^{+0.14}_{-0.17}$	$0.87^{+0.29}_{-0.26}$	$0.73^{+0.15}_{-0.16}$	−0.071/−0.072/0.018	0.065/−0.14/0.03	0.0089/−0.22/0.89
R_{21}^{18}[d]	65	$1.42^{+0.64}_{-0.76}$	$1.57^{+0.47}_{-0.63}$	$1.4^{+0.72}_{-0.83}$	…	…	…
$R_{10}^{13/12}$	2001	$0.12^{+0.03}_{-0.03}$	$0.15^{+0.03}_{-0.03}$	$0.12^{+0.025}_{-0.027}$	−0.016/−0.9/0.56	0.07/−0.82/2.1 × 10^{-5}	−0.26/−0.55/3.7 × 10^{-6}
$R_{21}^{13/12}$	301	$0.13^{+0.02}_{-0.03}$	$0.15^{+0.03}_{-0.03}$	$0.12^{+0.021}_{-0.025}$	−0.057/−0.95/0.014	0.10/−0.09/0.01	−0.0058/−1/0.94
$R_{10}^{18/13}$	857	$0.24^{+0.04}_{-0.04}$	$0.25^{+0.04}_{-0.04}$	$0.23^{+0.039}_{-0.046}$	−0.07/−0.59/0.021	0.038/−0.62/0.045	0.014/−0.7/0.84
$R_{10}^{18/12}$	857	$0.03^{+0.01}_{-0.01}$	$0.04^{+0.01}_{-0.01}$	$0.029^{+0.0085}_{-0.0093}$	−0.1/−1.5/0.085	0.081/−1.5/0.0049	−0.24/−1.3/0.02

Note.
[a] Number of significantly detected sight lines.
[b] The mean weighted by the ^{12}CO(1–0) integrated intensity. We also provide the weighted 16th-to-84th percentile range.
[c] We compute the slope, intercept, and Pearson p value of the linear regression fit to the stacked trend in log-log space.
[d] The high line ratio averages are most likely reflecting a significant observing bias due to the low sensitivity of the C^{18}O(2–1) observations, for which low ratios are censored.
[e] Discussed and presented in more detail in I. Galić et al. (2024, in preparation).

quantify any trends of the line ratio present with galactocentric radius, SFR surface density, nor ^{12}CO(1–0) line FWHM.

3.1.4. $R_{10}^{13/12}$ Ratio

For $R_{10}^{13/12}$, we measure a weighted-average and 16th-to-84th percentile range of $\langle R_{10}^{13/12}\rangle^{\rm weight.} = 0.12^{+0.03}_{-0.03}$. This is in agreement with the distribution of values of $\langle R_{10}^{13/12}\rangle^{\rm weight.}_{\rm lowres} = 0.12^{+0.02}_{-0.02}$ found for M51 at low angular resolution (dB22). At 33″ resolution, the ratio shows a mild decreasing trend with radius. With our high angular resolution observations, we see the radial line ratio trend has three distinct regimes: the ratio sharply increases with radius out to 0.6 kpc. Such a trend has been reported by the previous studies by T. Tosaki et al. (2002), although their ratio is a factor of 2 lower (they report $R_{10}^{13/12}\sim$ 0.05–0.1). For radii $\geqslant$0.6 kpc, the ratio then decreases as function of radius. From 0–0.6 kpc, the slope of the trend amounts to $m = 0.25$. At $\geqslant$0.6 kpc, the slope then changes to $m = -0.04$. Finally, at $r > 2$ kpc, where the transition from the central region to the onset of the spiral arms occurs, the ratio again mildly increases.

We also detect an increasing trend of $R_{10}^{13/12}$ with SFR surface density. A linear regression of the stacked trend in log-log space (orange line) yields a slope of $m = 0.07$ (p value of 2.1×10^{-5}), which is comparable to the slope of the correlation of R_{21}^{13} with the SFR surface density. Finally, the stacked line ratio trend does show a significant negative correlation with the ^{12}CO(1–0) line FWHM. We find a decreasing slope of $m = -0.27$ (the p value $\ll$0.01) in log-log space.

3.1.5. $R_{21}^{13/12}$ Ratio

For $R_{21}^{13/12}$, we measure higher values than reported by dB22 at coarse angular resolution. The luminosity weighted average and 16th-to-84th percentile range at 4″ resolution is $\langle R_{21}^{13/12}\rangle^{\rm weight.} = 0.13^{+0.03}_{-0.03}$. For comparison, the distribution reported at 33″ is $\langle R_{21}^{13/12}\rangle^{\rm weight.}_{\rm lowres} = 0.09^{+0.01}_{-0.02}$. The ratio shows a mild decrease with increasing radius (slope of $m = -0.06$ with p value of 0.01). We do detect a mildly increasing ratio trend between 0 and 0.6 kpc, similar to the $R_{10}^{13/12}$ trend. The stacked ratio trend correlates positively with the SFR surface density. In log-log space, we measure for the stacked line ratio trend a slope of $m = 0.1$. This correlation is comparable to the other line ratio trends we measure. Finally, $R_{21}^{13/12}$ does not show any correlation with the FWHM of ^{12}CO(1–0) nor ^{12}CO(2–1) (not shown here): neither its stacked trend nor the individual significantly detected sight lines.

3.1.6. $R_{10}^{18/13}$ Ratio

Because the emission of both line transitions of $R_{10}^{18/13}$ is optically thin, this ratio makes it possible to directly trace any change of the relative abundances of the ^{13}CO and C^{18}O species. This particular ratio is studied and discussed in detail in Galić et al. (2024, in preparation), and we refer the reader to this publication for more details. Qualitatively, this ratio shows, similarly to $R_{10}^{13/12}$, a decreasing trend toward the center at $r_{gal} < 1$ kpc. The ratio also decreases then again with increasing radius.

3.2. Molecular Gas Conditions Under LTE-assumption

Assuming LTE, optically thick ^{12}CO, and optically thin ^{13}CO emission, we can use analytic expressions to derive the excitation temperature from ^{12}CO and the optical depth and column density using ^{13}CO. We choose ^{13}CO over the other optically thin tracer C^{18}O because of the higher respective S/N of the line. In summary, we use the following specific assumptions (T. L. Wilson et al. 2009):

1. For a given sight line, the excitation temperature, T_{ex}, is uniform for all rotational-J transitions.
2. The excitation temperature is the same for all CO isotopologues.
3. The emission of both ^{12}CO(1–0) and (2–1) is optically thick ($\tau \gg 1$).
4. The ^{12}CO and ^{13}CO line emission originates from the same volume, as described by an identical beam filling factor, ϕ.

These assumptions do not necessarily represent the real conditions in the ISM but can provide a quick and straightforward constraint on the gas density, temperature, species abundances, and line optical depths (see Section 3.3 for our

non-LTE calculations). The LTE approach is often performed in the literature in the Milky Way and nearby galaxies (e.g., R. L. Dickman 1978; A. Nishimura et al. 2015; D. Cormier et al. 2018; A. Roueff et al. 2021; C. Wang et al. 2023). Therefore, we will first focus on these assumptions, and provide a comparison to the results of other studies.

We start with the following Equations (15)–(29) from T. L. Wilson et al. (2009), which relates the peak temperature, $T_{\rm peak}$, of a line and the excitation temperature, $T_{\rm ex}$:

$$T_{\rm peak} = \phi\,(1 - e^{-\tau})\frac{h\nu}{k_{\rm B}}\left[\frac{1}{e^{h\nu/k_{\rm B}T_{\rm ex}} - 1} - \frac{1}{e^{h\nu/k_{\rm B}T_{\rm CMB}} - 1}\right], \tag{2}$$

where ϕ is respective the beam filling factor, τ is the optical depth, h is the Planck constant, $k_{\rm B}$ is the Boltzmann constant, ν is the rest-frame frequency, and $T_{\rm CMB}$ is the cosmic microwave background temperature of 2.71 K. Then, under the set of assumptions outlined above, we proceed as follows:

1. We apply Equation (2) to our ^{12}CO(1–0), ^{12}CO(2–1) and ^{13}CO(1–0) line measurements. This yields three equations and three measurements (the peak brightness temperatures) for each line of sight.
2. From this system of equations, we still remain with four unknowns: a common filling factor, a common $T_{\rm ex}$, and the ^{12}CO(1–0) and ^{13}CO(1–0) opacities.[32]
3. However, under the assumption of optically thick ^{12}CO(1–0) and (2–1) emission, the term $e^{-\tau}$ will tend to 0, reducing the system to three unknown parameters.
4. We infer $T_{\rm ex}$ and the filling factor from the two ^{12}CO equations and use them to determine the ^{13}CO opacity.
5. Additionally, under reasonable assumptions of the [^{12}CO]/[^{13}CO] abundance ratio, we can crosscheck that the assumption of ^{12}CO opacity $\gg$1 is justified.

The optical depth of ^{13}CO is then computed using the following equation:

$$\tau_{^{13}\rm CO} = -\ln\left[1 - \frac{T^{13}_{\rm peak}}{\phi h\nu/k_{\rm B}}\left\{\frac{1}{e^{\frac{h\nu}{k_{\rm B}T_{\rm ex}}} - 1} - \frac{1}{e^{\frac{h\nu}{k_{\rm B}T_{\rm CMB}}} - 1}\right\}^{-1}\right]. \tag{3}$$

Using this estimate of the optical depth, τ, for ^{13}CO, we can further calculate the entire column density of all level populations of ^{13}CO along each sight line. The (beam-averaged) column density of ^{13}CO relates to the excitation temperature, the ^{13}CO(1–0) line center optical depth, and the integrated ^{13}CO(1–0) intensity, $W_{^{13}\rm CO(1-0)}$ as follows (T. L. Wilson et al. 2009):

$$N_{\rm LTE}(^{13}\rm CO)\,[\rm cm^{-2}] = 3.0\times10^{14}\cdot\frac{1}{1 - e^{-5.3/T_{\rm ex}}}\cdot\frac{\tau_{^{13}\rm CO}}{1 - e^{-\tau_{^{13}\rm CO}}}\cdot W_{^{13}\rm CO(1-0)}. \tag{4}$$

We present the distribution of values from our LTE-based calculations in Figure 5 and investigate trends in Figure 6. We additionally assess the measurement uncertainty associated with individual data points, which we illustrate in the bottom-right corner of each panel of Figure 6. This is achieved through a Monte Carlo (MC) resampling procedure conducted 100 times, wherein we systematically introduce the measured intensity's uncertainty and reiterate the LTE-modeling process. Subsequently, we quantify the uncertainty by calculating the standard deviation across the 100 iterations for all modeled quantities.

3.2.1. Excitation Temperature in M51

We present the derived excitation temperature in the top- and bottom-left panels of Figure 5. The map showcases the spatial distribution of $T_{\rm ex}$. Qualitatively, we do not find any clear spatial trends apart from a slight increase toward the downstream region of the southern spiral arm, where heating from young stars could play a role, and in the central northern region, the values also are higher than in the spiral arm. The bottom-left panel of Figure 5 presents the distribution of the values across the mapped region of M51. We measure a mean and 16th-to-84th percentile range of $\langle T_{\rm ex}\rangle = 7.5^{+5.4}_{-2.3}$ K. While most temperatures have $T_{\rm ex} < 10$ K (80% of the sight lines), there is a small tail toward higher excitation temperatures exceeding 10 K, indicating regions of more extreme excitation conditions. We note again that sight lines where the ^{12}CO(2–1)/(1–0) peak temperature ratio exceeds unity (2% of sight lines) are excluded from the subsequent analysis. Such sight lines require accounting for non-LTE effects, which is part of the analysis presented in Section 3.3.

3.2.2. The Beam Filling Factor for ^{12}CO

The top-middle and bottom-second-to-left panels in Figure 5 present the distribution of derived ϕ-values. We note that 5% of the sight lines show a beam filling factor larger than unity. This likely indicates that, in general, one or more of the assumptions listed at the beginning of this subsection, are not fully met for these sight lines. Assessing qualitatively the top-middle panel in Figure 5, we see that the beam filling factor reaches values close to unity along the central spine of the spiral arm and decreases toward its edges. In the interarm region, the beam filling factor is consistently below unity. Overall, we find a peak in the ϕ-distribution between 0.1 and 0.3, and a piling up of values at 1 (which is artificially induced, as we cap the beam filling factor at unity).

3.2.3. The Optical Depth of ^{13}CO

In the subsequent analysis, we focus on the optical depth derived using the ^{13}CO(1–0) emission line according to Equation (4). The overall distribution of $\tau_{^{13}\rm CO}$ is represented in the bottom-middle panel in Figure 5. We note that apart from a small fraction (6% in area), it is less than unity everywhere across the galaxy at 4″ (∼170 pc) scales. We find a mean of $\langle\log_{10}(\tau_{^{13}\rm CO})\rangle = -0.8^{+0.6}_{-0.5}$. Forty-four percent of sight lines have an optical depth of $\log_{10}(\tau_{^{13}\rm CO}) < -1$, which we consider to be the threshold for optically thin emission. A large part of the optical depth therefore is neither optically thin nor optically thick, but lies in the regime between. These elevated opacities suggest potential limitations of ^{13}CO as a tracer of the entire column of gas along the line of sight. As a consistency check, assuming a [^{12}CO]/[^{13}CO] abundance ratio of 30 for M51 (e.g., E. Schinnerer et al. 2013, which is consistent with the value we find using the non-LTE approach; see Section 3.3),

[32] We note that, technically, we have another unknown parameter: the opacity of ^{12}CO(2–1). However, for the purposes of these calculations, we only require ^{12}CO(1–0) and ^{12}CO(2–1) to be optically thick and do not derive any estimates of the optical depth for ^{12}CO(2–1) itself.

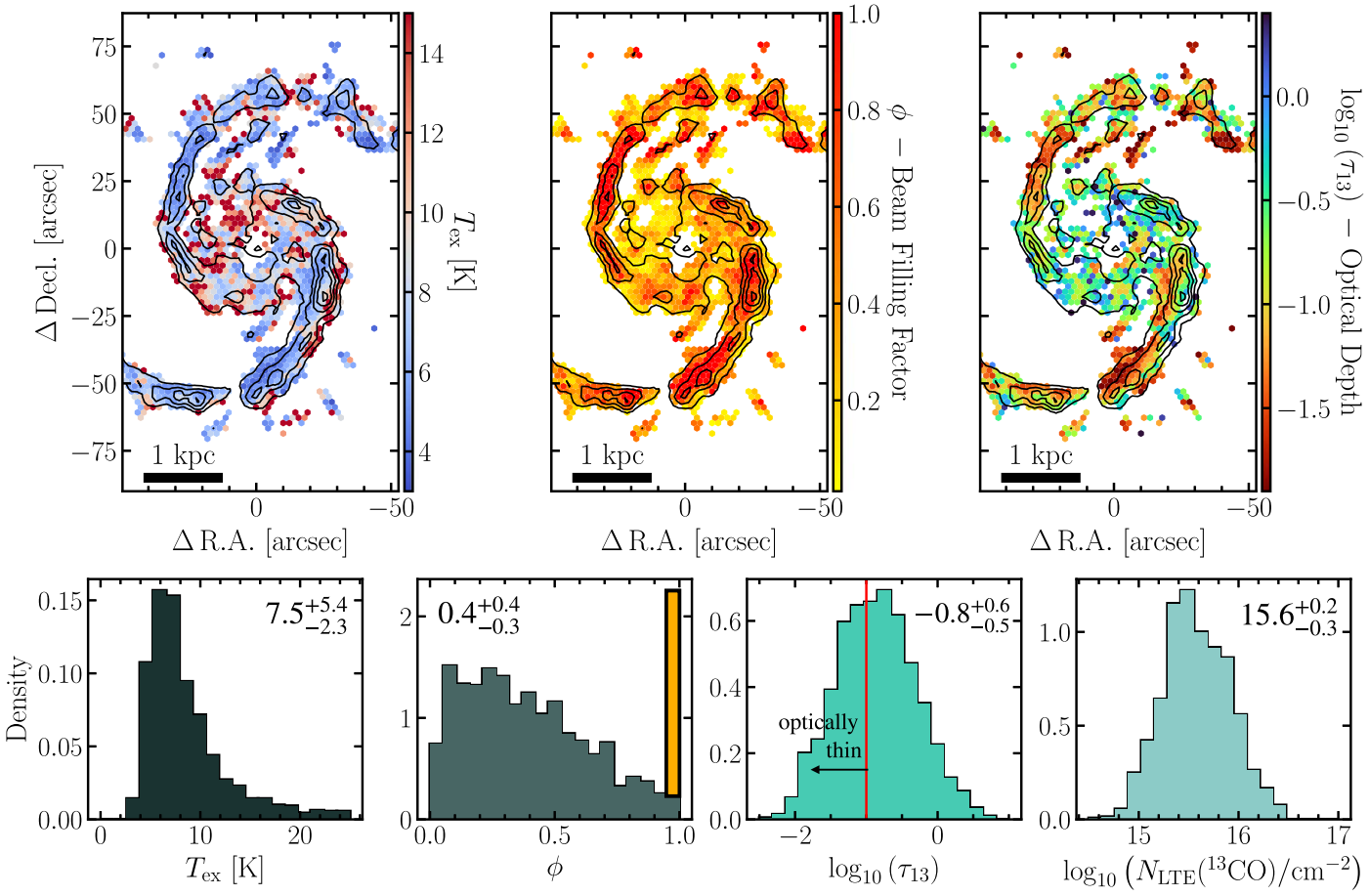

Figure 5. Distribution of LTE-derived parameter values. (Top row panels) The maps illustrate the distribution of the excitation temperature, T_{ex} (left panel), the beam filling factor, ϕ (center panel), and the ^{13}CO optical depth (right panel), across the inner region of M51. The contours indicate the ^{12}CO(1–0) integrated intensities ranging from 40–200 K km s^{-1} in steps of 40 K km s^{-1}. (Bottom row panels) The panels present the distribution of the excitation temperature (T_{ex}), the beam filling factor (ϕ), the optical depth of ^{13}CO (τ_{13}), and the ^{13}CO column density ($N_{LTE}(^{13}CO)$). The median and 16th-to-84th percentile range are indicated in the upper corner of each panel. The beam filling factor is set to 1 if the derived value exceeds unity. This causes a pile-up (indicated in orange) in the distribution. Optical depth values below $\log_{10}(\tau) < -1$ (left of the red vertical line) can be considered as optically thin.

67% of sight lines have an optical depth $\tau > 2$, implying optically thick ^{12}CO emission.

3.2.4. The ^{13}CO Column Density and α_{CO}

In the left panel of Figure 6, we present the LTE-derived ^{13}CO column densities using Equation (4) as a function of SFR surface density (based on the 33 GHz continuum emission). The two quantities appear to correlate (Pearson's p value $\ll 0.05$). This is particularly evident if we fit a linear regression to the sight lines within the 80% inclusion region (indicated by the red contour in the panel). The observed positive correlation between column density and SFR surface density is in line with the Schmidt–Kennicutt relation (M. Schmidt 1959; R. C. Kennicutt & N. J. Evans 2012), which connects the surface density of (molecular) gas with the SFR. We note, however, that the slope is shallower than the one found for Σ_{SFR} and Σ_{mol} in M51 (F. Bigiel et al. 2008 reported a slope of ∼1.2). Directly comparing the Schmidt–Kennicutt relation is challenging, as the derived slope is affected when applying different sensitivities and depends on the treatment of upper limit. Therefore, although our approach estimates the column density differently—using LTE modeling rather than applying a constant CO-to-H_2 conversion factor to CO intensities—as is commonly done in the literature, the correlation between the ^{13}CO column density and the SFR surface density remains robust. Therefore, this suggests that the column density derived from our method still effectively traces the mass distribution of molecular gas.

Therefore, using a fiducial ^{13}CO-to-H_2 abundance ratio, we can also translate the ^{13}CO column density into an estimate for the H_2 column density. More generally, we are interested in establishing an estimate for the CO-to-H_2 conversion factor ($\alpha_{^{12}CO(1-0)}$, hereafter just abbreviated as α_{CO}), which is defined as the ratio of molecular gas surface density to the integrated ^{12}CO(1–0) intensity (A. D. Bolatto et al. 2013). Following J. Kamenetzky et al. (2014) and Y.-H. Teng et al. (2022), we can derive the following functional form for the conversion factor as function of the ^{13}CO column density:

$$\alpha^{LTE}_{^{12}CO(1-0)} = \frac{1}{4.5 \times 10^{19}} \frac{N(^{13}CO)/[^{13}CO/H_2]}{W_{^{12}CO(1-0)}}. \quad (5)$$

The derivation of the conversion factor depends on the assumed abundance ratio. For this analysis, we assume an abundance of $[^{13}CO/H_2] = 1.7 \times 10^{-6}$ (R. L. Dickman 1978). We note, however, that the abundance ratio varies within galaxies (e.g., M. A. Frerking et al. 1982; P. F. Goldsmith et al. 2008; K. Sliwa et al. 2012) by up to an order of magnitude with a typical scatter around 0.5 dex for a fixed H_2 density (E. F. van Dishoeck et al. 1992; Y. Sheffer et al. 2008). At cloud-scales,

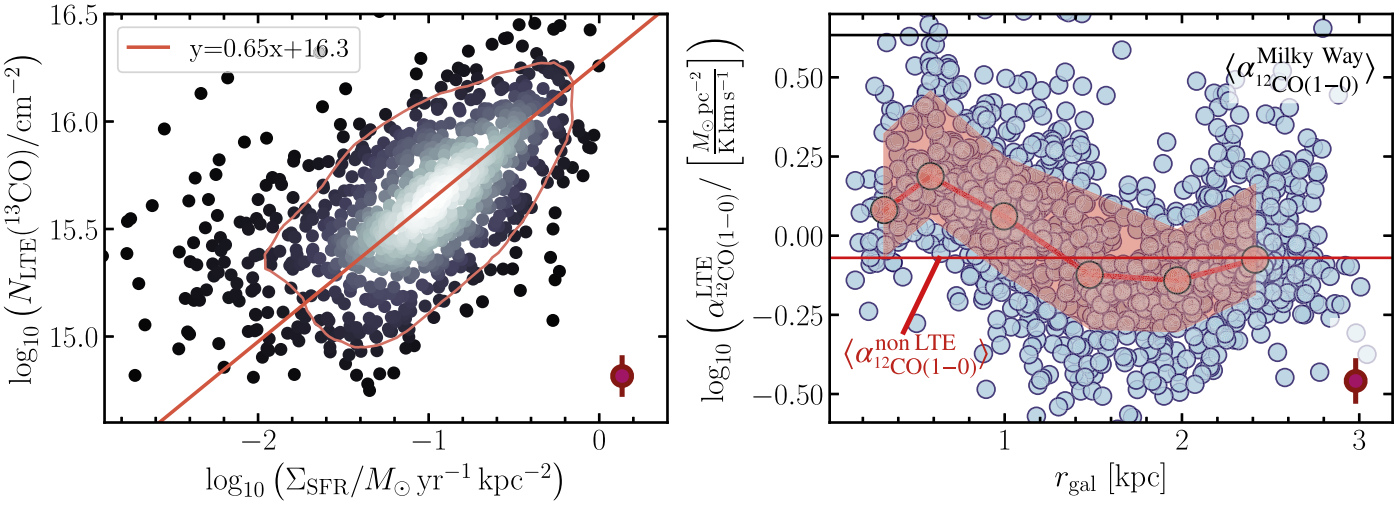

Figure 6. Correlations of the LTE-based parameters. (Left panel) We compute the ^{13}CO column density, $N_{\rm LTE}(^{13}{\rm CO})$ based on the ^{13}CO(1–0) integrated intensity using Equation (4), which assumes LTE. Only sight lines were used where the ^{13}CO(1–0) line emission is significantly detected (S/N $\geqslant$ 5). (Right panel) The CO-to-H_2 conversion factor for the ^{12}CO(1–0) emission as a function of galactocentric radius assuming $[^{13}{\rm CO}/{\rm H_2}]=1.7\times10^{-6}$. The red circles show binned values. The shaded red area represents the $\pm1\sigma$ scatter per bin. For reference, we also present the local neighborhood value of 4.3 (black line) and the average value derived from our non-LTE analysis (red line). In the bottom-right corner of each panel, we present the average error for a single data point, based on the MC resampling approach. In the left panel, points are color-coded based on their density in the panel (this is a qualitative representation of how densely the points are distributed in the parameter space).

we do not resolve the molecular clouds; therefore, the beam-to-beam variations of the abundance are expected to be smaller. Furthermore, within the central $r\leqslant3$ kpc region, which we analyze here, we do not expect such large variations, as large variations in the ^{13}CO abundance are mostly related to lower metallicity and lower (column) density regimes, such as the outskirts of galaxies.

The right panel of Figure 6 illustrates the derived conversion factor as a function of galactocentric radius. We find a mean conversion factor distribution and a corresponding 1σ scatter per bin/region of $\langle\alpha^{\rm LTE}_{^{12}{\rm CO}(1-0)}\rangle = 1.0^{+0.2}_{-0.2}\,M_\odot\,{\rm pc}^{-2}/({\rm K\,km\,s}^{-1})$. The values toward the center ($r_{\rm gal}<0.2$ kpc) are significantly lower with $\langle\alpha^{\rm LTE}_{^{12}{\rm CO}(1-0),{\rm center}}\rangle = 0.48^{+0.03}_{-0.03}\,M_\odot\,{\rm pc}^{-2}/({\rm K\,km\,s}^{-1})$. The conversion factor increases with radius up to $\sim$0.5 kpc. At larger radii, we measure a negative correlation with galactocentric radius. We note two things in particular when comparing the derived conversion factor relation to the one described in J. S. den Brok et al. (2023b) at coarser, kiloparsec-scale resolution: (i) our average CO-to-H_2 conversion factor is $\sim$3 times lower (they report a value of 3.1 $M_\odot\,{\rm pc}^{-2}/({\rm K\,km\,s}^{-1})$ for the central 2 kpc in radius); and (ii) they do not report a lower conversion factor toward the center. In their study, J. S. den Brok et al. (2023b) measured the conversion factor using a dust-based approach to estimate independently the H_2 mass distribution. Lower systematic ^{13}CO-based conversion factors have been found before; e.g., D. Cormier et al. (2018) found, on average, a factor of 2 lower-than-the-Milky-Way value for their sample of galaxies. It is worth noting that the conversion factors based on ^{13}CO are predicted to be offset by a factor of 2–3 by simulations (e.g., L. Szűcs et al. 2016), which would bring our values and the dust-based values closer in agreement. One explanation for this is that the excitation temperatures for the different species can differ. Looking at Equation (4), the conversion factor scales approximately linearly with excitation temperature (for optically thin lines). Finally, we also have not considered any gradient in the ^{13}CO-to-H_2 abundance ratio, which could explain the discrepancy as well. A linear relation of the $^{12}{\rm CO}/{\rm H_2}$ abundance with metallicity is expected from theoretical considerations (S. Bialy & A. Sternberg 2015), but over the small radial range we cover in M51, such a gradient is not significant. For instance, D. A. Berg et al. (2020) reported a radial metallicity gradient of 0.2 dex over the entire disk of M51. This suggests only gradients and changes in the relative $^{12}{\rm CO}/^{13}{\rm CO}$ abundance ratio remain relevant. For a more robust approach, which takes differences in the excitation temperature and varying ^{12}CO-to-^{13}CO abundance ratios into consideration, we require non-LTE computations.

3.3. Beyond LTE: Modeling the Line Emission by Solving the Non-LTE Radiative Transfer Equations

As an alternative approach to the LTE-based calculations, we employ the non-LTE radiative transfer code RADEX (F. F. S. van der Tak et al. 2007) to model the observed line intensities. Here, we follow the framework presented in Y.-H. Teng et al. (2022, 2023), and refer the reader to these publications for details and background on the RADEX implementation. The free parameters that we model are the permutations of a range of kinetic temperature ($T_{\rm kin}$), H_2 volume density ($n_{\rm H_2}$), ^{12}CO column density per line width ($N_{\rm CO}/\Delta v$), the $^{12}{\rm CO}/^{13}{\rm CO}$ abundance ratio ($[^{12}{\rm CO}/^{13}{\rm CO}]$), and the beam filling factor (ϕ). As input for the energy levels, statistical weights, Einstein A, and collisional rate coefficients of each CO isotopologue, we use the data files from the Leiden Atomic and Molecular Database (LAMDA; F. L. Schöier et al. 2005), which provide collisional rate coefficients from B. Yang et al. (2010). We note that R. Tunnard & T. R. Greve (2016) showed that such a model setup can recover the physical conditions of the molecular gas using CO isotopologues. For the non-LTE line modeling, we do not include the C^{18}O (1–0) and (2–1) lines, as the (2–1) observations have a low sensitivity and hence would limit the analysis to a very small number of sight lines.

We run `RADEX` by creating first a 4D grid with the grid points specified as ($T_{\rm kin}$, $n_{\rm H_2}$, $N_{\rm CO}/\Delta v$, $[^{12}{\rm CO}/^{13}{\rm CO}]$). We then expand this grid to five dimensions by multiplying the

Table 3
RADEX-model Parameters

Parameter	Range	Step Size
$T_{\rm kin}$	4–100 K	2 K
$\log_{10}(n_{\rm H_2}/{\rm cm}^{-3})$	2–5	0.2 dex
$\log_{10}(N_{^{12}{\rm CO}}/{\rm cm}^{-2})$	16–20	0.2 dex
$[^{12}{\rm CO}/^{13}{\rm CO}]$	20–80	10
Δv	15 km s^{-1}	...
$\log_{10}(\phi)$	−2–0	0.2 dex

intensities by a range of beam filling factors (ϕ). For this model, we assume that these conditions are uniform for a given line of sight. The range of kinetic temperature, H_2 density, CO column density, and abundance ratio used to build the grid is presented in Table 3. Moreover, for the $N_{\rm CO}/\Delta v$ parameter, we use a fixed line width of $\Delta v = 15$ km s^{-1}. While we expect the line width to scale with the size of the GMCs (M. H. Heyer & C. M. Brunt 2004), at a resolution of ∼120 pc, we can hardly resolve the clouds. The line width of ∼15 km s^{-1} is hence empirically motivated (see Figure 3).[33] In total, this grid amounts to ∼ 260,000 grid points. We provide the entire machine-readable parameter grid in Appendix C.

We perform a χ^2 minimization to determine which grid point best represents the molecular conditions that produce the observed CO isotopologue line emission per sight line. We compute χ^2 for the grid point $\theta = (T_{\rm kin}, n_{\rm H_2}, N_{\rm CO}/\Delta v, [^{12}{\rm CO}/^{13}{\rm CO}], \phi)$ for the $n = 4$ lines (the two lowest rotational-J transitions for ^{12}CO and ^{13}CO) using the following expression:

$$\chi^2(\theta) = \sum_{i=1}^{n} \left(\frac{W_i^{\rm model}(\theta) - c_i^{\rm line} \cdot W_i^{\rm obs}}{\sigma_i^{\rm obs}} \right)^2 \quad (6)$$

where $c_i^{\rm line}$ captures the adjustment of the line width. We use $c_i^{\rm line} = 15$ km s^{-1}/FWHM$_i$. In Equation (6), $W_i^{\rm model}$ and $W_i^{\rm obs}$ represent the modeled and observed integrated intensity of the ith line, respectively. We adjust the modeled intensity by the beam filling factor of the line, ϕ_i, which we vary from 0.01–1 in logarithmic steps of 0.2 dex. We assume an "n" identical beam filling factor for both the ^{12}CO and ^{13}CO emission lines. The observational uncertainty is captured in the equation by the parameter σ_i. For the purpose of the χ^2 minimization approach, we use, in addition to the noise uncertainty, a conservative estimate of 10% uncertainty on the measured intensity, reflecting the calibration uncertainty, which is commonly adopted in the literature (e.g., A. K. Leroy et al. 2017a; Y.-H. Teng et al. 2022). To quantify the significance of the minimum χ^2, we compute for each grid point a likelihood probability, assuming a multivariate Gaussian probability distribution:

$$P(W^{\rm obs}|\theta) = \left(\prod_i^n (2\pi\sigma_i^2)^{-\frac{1}{2}} \right) \cdot e^{-\frac{1}{2}\chi^2(\theta)}. \quad (7)$$

[33] In essence, we fit $N_{\rm CO}/\Delta v$ with RADEX, instead of fitting $N_{\rm CO}$ and Δv separately. The actual estimation of $N_{\rm CO}$, hence, varies with the line widths. Therefore, where we provide estimates of $N_{\rm CO}$ values, we multiply $N_{\rm CO}/\Delta v$ with either ∼15 km s^{-1} for the modeled column density, or with the observed CO(1–0) line width for each pixel.

We attribute to each sight line the parameter combination based on the marginalized 1D likelihoods. For the RADEX grid parameters, which are sampled uniformly, the marginalized 1D likelihood distribution is obtained by summing over all likelihoods per fixed parameter. To derive the marginalized likelihoods of the ^{12}CO and ^{13}CO optical depths and $\alpha_{\rm CO}$, which are functions of the intrinsic grid parameters and possibly not regularly sampled, we proceed slightly differently. We produced a probability-weighted histogram based on the likelihoods for the optical depths. To account for the irregular sampling, we normalize this histogram by the uniformly weighted histogram. We note that this approach is consistent with the approach described in Y.-H. Teng et al. (2022).

Figure 7 illustrates the method for two arbitrarily selected pixels of the map. The corner plots depict the 1D and 2D probability density function (PDF) distribution (Equation (7)). The 1D and 2D PDFs are derived from the 5D PDF (since we have five free parameters) by summing along the remaining axes. In essence, we use four observed emission lines to derive constraints on five free parameters. This is possible because the χ^2 minimization approach quantifies the probability of every combination of model parameters given the data. Such an approach is well established in the astronomy-applied statistics literature (e.g., Ž. Ivezić et al. 2014). The derived "best-fit" parameters are then estimated by marginalizing over these likelihood distributions. This differs from the classical fitting of the data where one can, for instance, analytically derive a "best-fit" parameter.

Figure 8 illustrates the spatial distribution of the derived physical quantities. Table 4 lists the intensity weighted averages and scatter. The 1D and 2D pdfs of these two selected pixels represent well the general behavior of the χ^2 minimization approach. Overall, the beam filling factor (ϕ), the volume density ($n_{\rm H_2}$), and ^{12}CO column density ($N_{^{12}{\rm CO}}$) are well constrained. The ^{12}CO-to-^{13}CO abundance ratio and the kinetic temperature ($T_{\rm kin}$), on the other hand, are less well constrained, as indicated by a wider distribution of values.

Similarly to the LTE line modeling approach, we estimate the uncertainty of an individual data point by resampling the data by adding noise to the intensities and repeating the non-LTE χ^2-minimization. The uncertainties are then determined for each quantity by taking the standard deviation along the 100 samples.

3.3.1. Comparison between LTE and Non-LTE-derived Properties

Using the non-LTE approach, we can directly compare the derived optical depth and the total column density of ^{13}CO to the LTE-based results (discussed in Section 3.2). We present the comparison in Figure 9. Note that we scale the RADEX-derived column densities by the beam filling factor, ϕ, such that both the LTE and non-LTE represent the beam-averaged column density. Furthermore, we correct the non-LTE value by the full observed ^{12}CO(1–0) line width instead of the fiducial 15 km s^{-1} line width.

Overall, the optical depth of ^{13}CO(1–0) (left panel) shows on average a distribution of values that is offset by 0.6 dex with respect to the LTE values, with non-LTE values having a mean of −0.2. For the total column density of ^{13}CO (right panel), the distributions also differ, as the non-LTE values are systematically higher by ∼0.2 dex. The correlation between LTE and non-LTE column densities suggests that to first order, the intensities are proportional to the column density, as expected

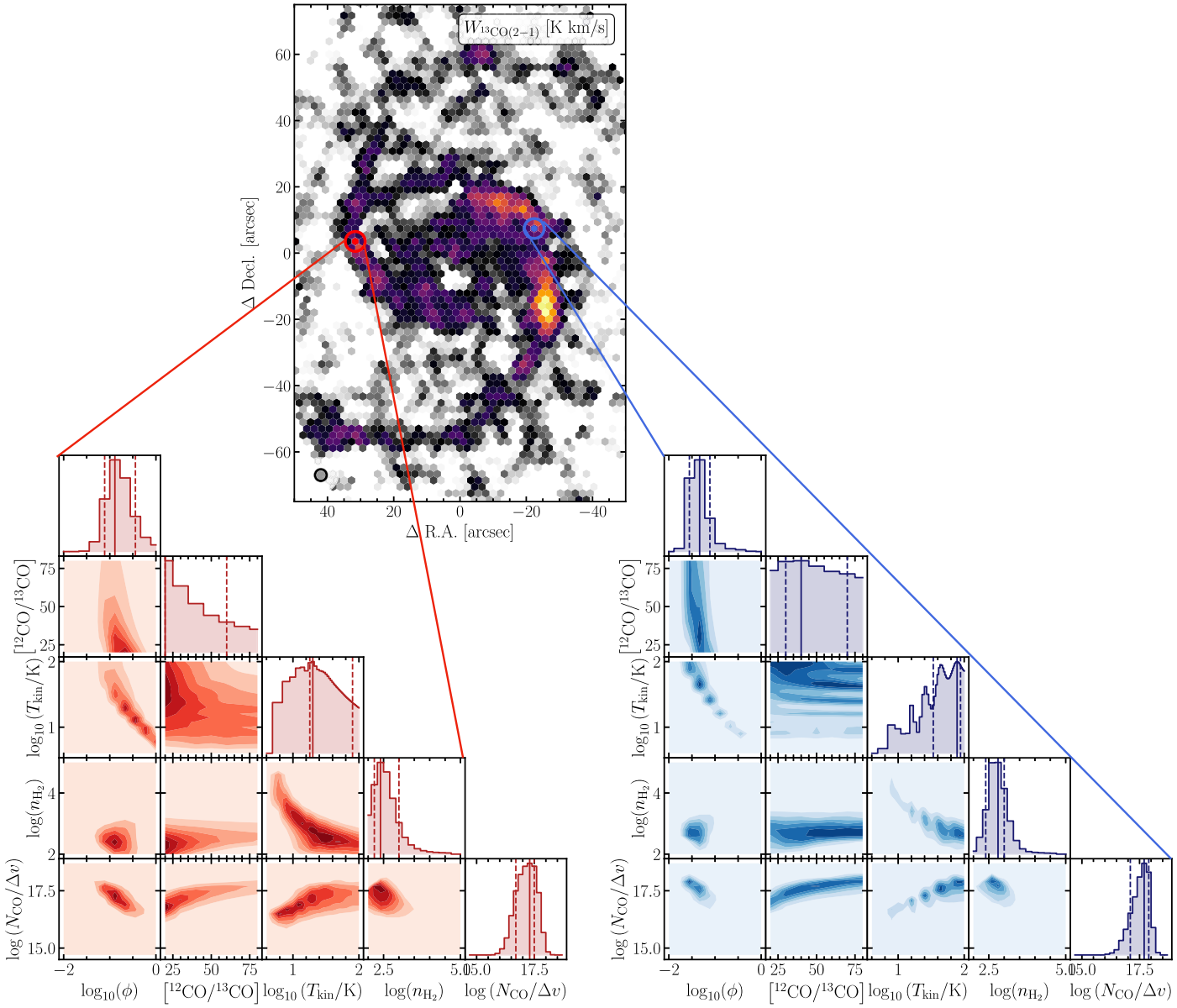

Figure 7. The 1D and 2D marginalized likelihood distributions. The red (left panel) and blue (right panel) corner plots show the resulting 1D and 2D likelihood probability density function (PDF) from χ^2 minimization following Equation (7). The map in the center illustrates the ^{13}CO(2–1) integrated intensity with the sight lines highlighted for which the two corner plots are calculated.

for a line that is not optically thick. In Table 5 we provide the mean and 16th-to-84th percentile range of the overall distribution of values of the optical depth and column density.

For the optical depth, we find that the non-LTE-based values are also $\tau_{^{13}CO}^{non-LTE} < 1$, indicating that the ^{13}CO line emission is not optically thick. However, the values are also $\tau_{^{13}CO}^{non-LTE} > 0.1$, indicating that the line neither is optically thin. This likely also explains to some degree why the LTE-derived column densities are offset by a factor of 2, as the assumption of optically thin emission is not necessarily true. The scatter of the overall distribution of values is significantly larger for the LTE-derived ones with ∼0.6 dex compared to ∼0.2 dex for the non-LTE-derived values. The larger scatter for LTE is expected since this approach has a lower number of free parameters, thereby limiting the ways the parameters can balance each other out.

The total ^{13}CO column density values of the overall distribution are systematically offset beyond the scatter for the LTE and non-LTE approach. The LTE-based mean and percentile range of $\langle \log_{10}(N_{LTE}(^{13}CO)/cm^{-2}) \rangle = 15.8^{+0.4}_{-0.3}$ is smaller than the non-LTE-based distribution of values of $\langle \log_{10}(N_{non-LTE}(^{13}CO)/cm^{-2}) \rangle = 16.0^{+0.2}_{-0.2}$. Using a linear regression fit in logarithmic space, we find a significant correlation with Pearson's $p \ll 0.05$.

The overall agreement or correlation between the LTE and non-LTE-derived averages of the column density suggests that any discrepancies of further parameters are likely due to differences in the initial assumptions (e.g., of a fixed ^{12}CO or the ^{13}CO-to-H_2 abundance ratio).

3.3.2. The ^{12}CO(1–0) Optical Depth and the ^{12}CO-to-H_2 Conversion Factor

From the non-LTE approach, we derive an estimate of the ^{12}CO(1–0) optical depth. We expect that the $R_{10}^{13/12}$ line ratio traces a combination of changes in the optical depth and

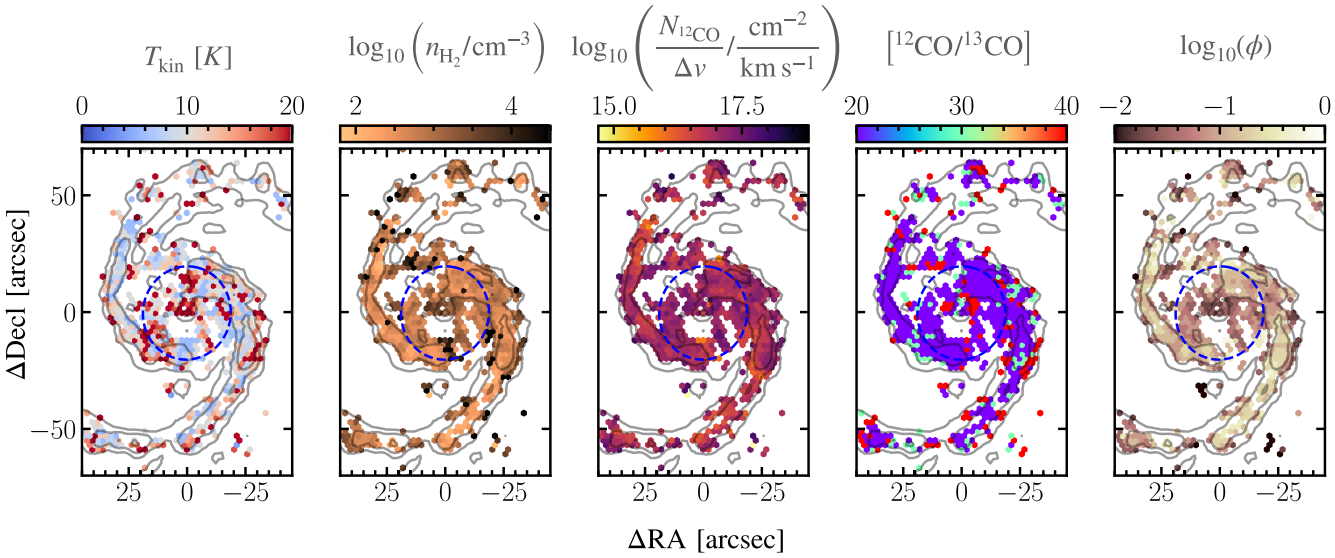

Figure 8. Spatial distribution of the maximum likelihood model. These panels show the pixel-wise maximum likelihood value derived from the χ^2 minimization approach. (Left panel) The kinetic temperature, $T_{\rm kin}$, map. The contours show the integrated ^{12}CO(1–0) intensity isophote at 20, 50, 100, and 200 K km s^{-1}. The blue-dashed circle indicates 20″ in radius, which we use to differentiate between center and disk. (Second-from-left panel) The distribution of the mean volume density, $n_{\rm H_2}$, from which the CO emission is originating. (Middle panel) The ^{12}CO column density map. (Second-from-the-right panel) The beam filling factor. (Right panel) The abundance ratio of ^{12}CO-to-^{13}CO map. We note that we only have solutions for pixels where all four lines (^{12}CO and ^{13}CO (1–0), (2–1)) are significantly (>5σ) detected.

Table 4
Non-LTE-based Intensity Weighted Averages

	All	Center	Disk
$\log_{10}(\tau_{^{12}{\rm CO}})$	$0.9^{+0.2}_{-0.3}$	$1.0^{+0.2}_{-0.2}$	$0.9^{+0.3}_{-0.2}$
$T_{\rm kin}$ [K]	13^{+5}_{-5}	17^{+3}_{-9}	12^{+4}_{-4}
$\log_{10}(n_{\rm H_2}/{\rm cm}^{-3})$	$2.8^{+0.6}_{-0.4}$	$2.9^{+0.3}_{-0.3}$	$2.7^{+0.7}_{-0.3}$
$\log_{10}\left(N_{^{12}{\rm CO}}/\Delta v\ \frac{\rm km}{{\rm cm}^{-2}\,{\rm km}^{-1}\,{\rm s}}\right)$	$16.9^{+0.4}_{-0.4}$	$17.0^{+0.3}_{-0.1}$	$16.9^{+0.4}_{-0.4}$
$[^{12}{\rm CO}/^{13}{\rm CO}]$	25^{+15}_{-5}	23^{+3}_{-3}	25^{+15}_{-5}
ϕ	$0.2^{+0.1}_{-0.2}$	$0.1^{+-0.1}_{-0.1}$	$0.2^{+0.2}_{-0.2}$
$\alpha^{\rm non-LTE}_{^{12}{\rm CO}(1-0)}\ \left[\frac{M_\odot\,{\rm pc}^{-2}}{{\rm K\,km\,s}^{-1}}\right]$	$2.4^{+0.7}_{-0.9}$	$2.7^{+0.8}_{-0.6}$	$2.3^{+0.9}_{-0.8}$

Note. The value corresponds to the ^{12}CO(1–0) intensity weighted average and 16th-to-84th percentile range. We differentiate also between center ($r_{\rm gal} \leqslant 20''$) and disk ($r_{\rm gal} > 20''$).

changes in the ^{12}CO-to-^{13}CO abundance ratio. To test the degree that the ratio traces changes in optical depth, we plot the optical depth against the $R_{10}^{13/12}$ line ratio in Figure 10. Based on a linear regression fit (in log-log space), we find a mild but significant positive correlation ($R_p = 0.41$, $p \ll 0.05$). The trend has a slope of 0.55 ± 0.2 for the correlation between $\log_{10}(R_{10}^{13/12})$ and $\log_{10}(\tau^{\rm non-LTE}_{^{12}{\rm CO}})$.

From the non-LTE model fits, we obtain an estimate of the ^{12}CO column density per line width, $N_{^{12}{\rm CO}}/\Delta v$ (where Δv corresponds to the line FWHM). We furthermore can determine a CO-to-H_2 conversion factor estimate for each grid point using the following formalism:

$$\alpha^{\rm non-LTE}_{^{12}{\rm CO}(1-0)}\left[\frac{M_\odot\,{\rm pc}^{-1}}{{\rm K\,km\,s}^{-1}}\right] = \frac{1}{4.5\ \times\ 10^{19}} \cdot \frac{1}{[^{13}{\rm CO}/{\rm H_2}]\cdot[^{12}{\rm CO}/^{13}{\rm CO}]} \cdot \frac{N(^{12}{\rm CO})}{W^{\rm model}_{^{12}{\rm CO}(1-0)}} \cdot \phi, \quad (8)$$

where the factor 4.5×10^{19} also considers helium. The accuracy of the derived CO-to-H_2 conversion factor also depends on the estimate of the ^{13}CO-to-H_2 abundance ratio [^{13}CO/H_2], which we convert into a ^{12}CO abundance ratio by multiplying with the derived [^{12}CO/^{13}CO] abundance ratio. We again rely on ^{13}CO-to-H_2 abundance ratio of 1.7×10^{-6}, which we employed already for the LTE analysis (see Section 3.2). Given our overall average [^{12}CO/^{13}CO] abundance ratio of ∼25, this translates into a ^{12}CO-to-H_2 abundance ratio of $\sim 0.4 \times 10^{-4}$. The final $\alpha_{\rm CO}$ estimate per line of sight is determined by taking the maximum of the normalized marginalized 1D PDF, similar to how we determine the non-LTE optical depth.

We plot the derived CO-to-H_2 conversion factor with respect to the galactocentric radius in Figure 11. The data points scatter around 0.3 dex. Assessing the trend qualitatively, we observe that the non-LTE-based conversion factor does show a flat radial trend with an indication of a decrease toward the center at radii smaller than $r_{\rm gal} < 0.5$ kpc. Taking from Table 4, we find the center ($r < 20''$) to have an average of $\langle\alpha_{^{12}{\rm CO}(1-0)}\rangle_{\rm center} = 2.7^{+0.8}_{-0.6}\ \frac{M_\odot\,{\rm pc}^{-2}}{{\rm K\,km\,s}^{-1}}$. Outside the center at larger radii, the value is slightly smaller with $\langle\alpha_{^{12}{\rm CO}(1-0)}\rangle_{\rm disk} = 2.3^{+0.9}_{-0.8}\ \frac{M_\odot\,{\rm pc}^{-2}}{{\rm K\,km\,s}^{-1}}$.

In comparison, on average, the non-LTE-based values are systematically larger by 0.3 dex (see Equation (5)). We also note that the average value of $\langle\alpha_{^{12}{\rm CO}(1-0)}\rangle = 3.1\ \frac{M_\odot\,{\rm pc}^{-2}}{{\rm K\,km\,s}^{-1}}$ reported by K. M. Sandstrom et al. (2013) for the nearby star-forming galaxy population falls within the scatter of our non-LTE-derived values. Moreover, J. S. den Brok et al. (2023b) found an identical value of $\langle\alpha_{^{12}{\rm CO}(1-0)}\rangle_{\rm den\ Brok+2023} = 3.2\ \frac{M_\odot\,{\rm pc}^{-2}}{{\rm K\,km\,s}^{-1}}$ for the central radial 1 kpc region, which is, again, the margin of scatter, which we find at high angular resolution with the non-LTE CO isotopologue line modeling.

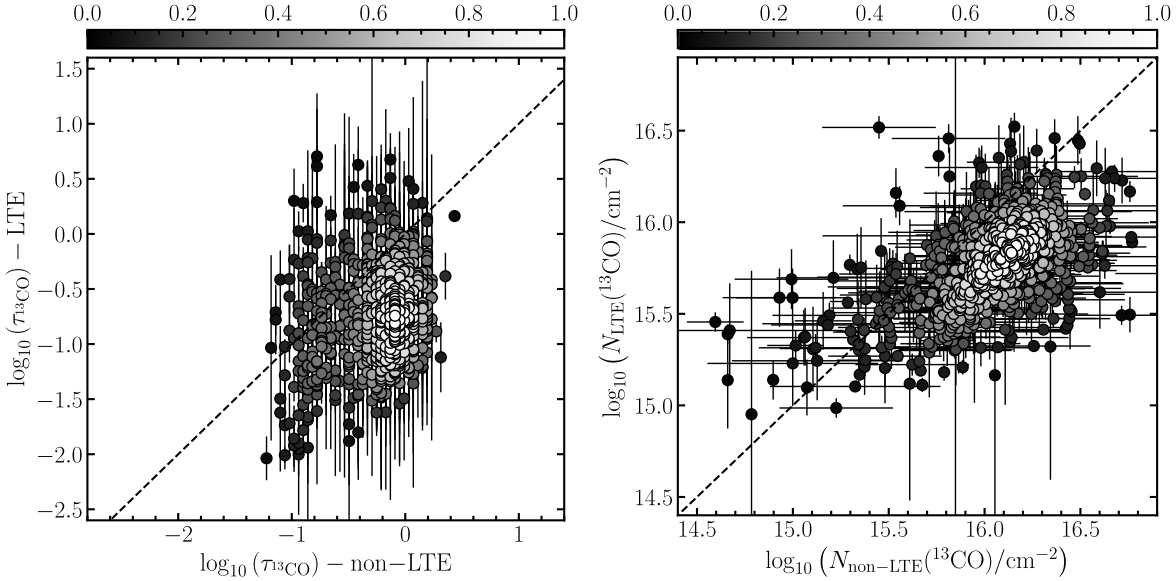

Figure 9. Comparing LTE and non-LTE-derived parameters. (Left panel) Contrasting the optical depth of ^{13}CO(1–0). The points are color-coded by their parameter-space filling based on a 2D Gaussian kernel function. The black dashed line illustrates the 1:1 relation. (Right panel) Comparing the total ^{13}CO column density derived using the LTE and non-LTE approach. The panel description follows the left one.

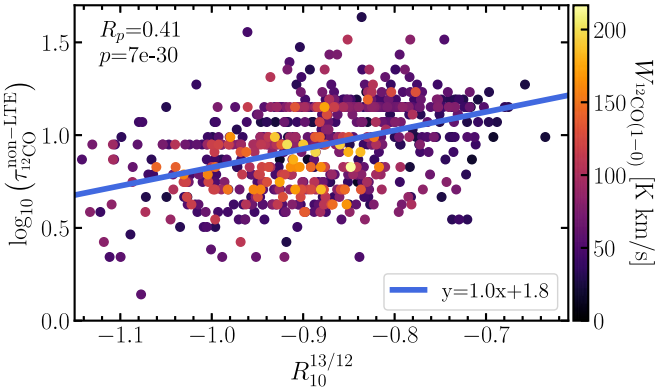

Figure 10. Optical depth of ^{12}CO and the $R_{10}^{13/12}$ line ratio. The points are color-coded with respect to the sight line's corresponding integrated ^{12}CO(1–0) line brightness. We perform a linear regression (in log-log space; blue line), which highlights the positive relation (Pearson's correlation coefficients indicated in top-left corner) with the $R_{10}^{13/12}$ line ratio.

Table 5
Comparing LTE and Non-LTE-based Results: The Mean and 16th-to-84th Percentile Range of the Overall Distribution of Values Presented in Figure 9

Parameter	LTE-based	Non-LTE-based
$\langle\log_{10}(\tau_{^{13}CO})\rangle$	$-0.9^{+0.6}_{-0.5}$	$-0.3^{+0.3}_{-0.3}$
$\langle\log_{10}(N(^{13}CO)/cm^{-2})\rangle$	$15.8^{+0.4}_{-0.3}$	$16.0^{+0.2}_{-0.2}$

In Figure 12, we contrast the conversion factor to the molecular gas velocity dispersion as traced by the FWHM of the ^{12}CO(1–0) line width. We find a weak ($R_p = -0.1$), but significant ($p \ll 0.05$) negative trend between the two quantities. For reference, we plot the galaxy-wide relation found by Y.-H. Teng et al. (2024) for a sample of 12 nearby galaxies, who report a slope of −0.81 using kiloparsec-scale dust $\alpha_{^{12}CO(1-0)}$ measurements and 150 pc scale Δv. For this comparison, we adjust the literature values such that the

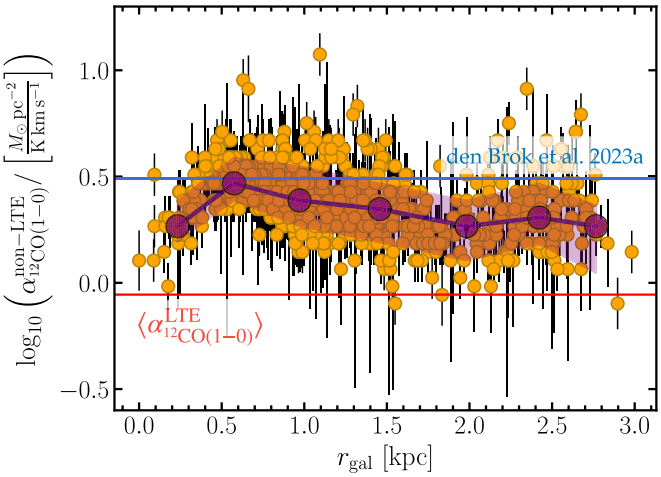

Figure 11. Radial trend of the non-LTE-derived CO-to-H_2 conversion factor. We find overall a flat trend of $\alpha_{^{12}CO(1-0)}$ with galactocentric radius. The orange points show the value for the individual sight lines. The purple points depict the radially binned average. We illustrate the scatter of the radially binned values using the purple shade. The galaxy-wide average based on a dust-based technique by J. S. den Brok et al. (2023b) is represented by the blue horizontal line. The red horizontal line represents our LTE-derived average α_{CO}.

CO-to-H_2 abundance ratio matches. Based on the average derived ^{12}CO-to-^{13}CO abundance ratio of 25 and the assumed ^{13}CO abundance of 1.7×10^{-6}, we find an average ^{12}CO abundance of 4×10^{-5}. To derive $\alpha_{^{12}CO(1-0)}$ using CO isotopologue measurements, Y.-H. Teng et al. (2023) assumed a ^{12}CO abundance of 3×10^{-4} for their sample of barred galaxy centers. In contrast, Y.-H. Teng et al. (2024) did not assume any abundance for their fit based on dust $\alpha_{^{12}CO(1-0)}$ measurements, but found that in order to match the Y.-H. Teng et al. (2023) results, the overall abundance appears to be 1.5×10^{-4}. Therefore, we scaled these trends to match our estimated CO-to-H_2 abundance. Using this scaling, we find that the trends described by Y.-H. Teng et al. (2023) and Y.-H. Teng et al. (2024) match well the distribution of values we find in M51.

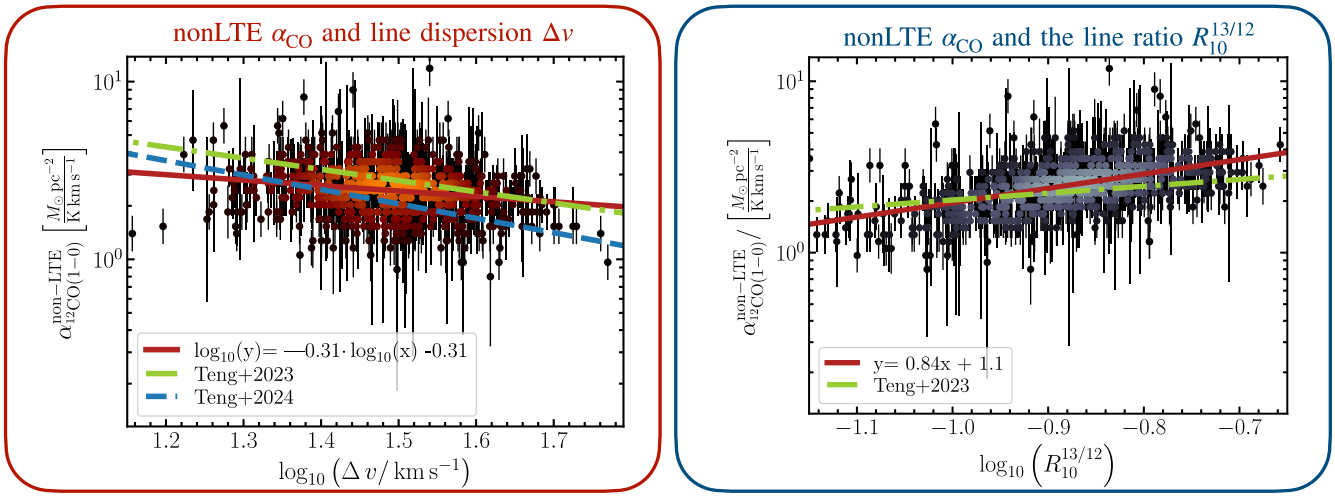

Figure 12. Analysis of the CO-to-H_2 conversion factor. (Left panel) The non-LTE-derived $\alpha_{^{12}CO(1-0)}$ correlated with the ^{12}CO(1–0) line dispersion. The red line indicates a regression fit. For reference, we also indicate the Y.-H. Teng et al. (2023) and Y.-H. Teng et al. (2024) regression fits (after accounting for differences in the assumed CO-to-H_2 abundance values) with the blue- and orange-dashed lines, which were obtained using a sample of three barred and 12 nearby star-forming galaxies, respectively. (Right panel) The non-LTE-derived $\alpha_{^{12}CO(1-0)}$ correlated with the observed ^{13}CO-to-^{12}CO ratio, $R_{10}^{13/12}$. The red line again shows a regression fit to the measurements of M51.

In the right panel of Figure 12, we show the trend with $R_{10}^{13/12}$. We find a mild ($R_p = 0.3$) and significantly ($p \ll 0.05$) positive correlation. A positive correlation is expected under the explanation that the $R_{10}^{13/12}$ ratio reflects changes in the optical depth, which, in turn, drives variation in α_{CO}. Y.-H. Teng et al. (2023) also reported a positive correlation with the ^{12}CO-to^{13}CO line ratio. We note that in their study, they correlated the conversion factor with the ratio for the 2–1 instead of the 1–0 transitions (i.e., $R_{21}^{13/12}$ instead of $R_{10}^{13/12}$). For reference, we plot the trend reported by Y.-H. Teng et al. (2023) in the panel as well (after adjusting for the difference in the CO-to-H_2 abundance, but not accounting for the fact that they provide it as a function of $R_{21}^{13/12}$ instead of $R_{10}^{13/12}$). Despite the use of different CO isotopologue transitions, the trend matches well our derived distribution of α_{CO}.

4. Discussion

4.1. Interpreting Global CO Isotopologue Line Ratio Trends

The implications of the varying CO isotopologue ratios have been qualitatively assessed in M51 at kiloparsec scales in dB22. Generally, we differentiate between two types of line ratios:

(a) line ratio of two different rotational-J transitions for the same CO isotopologue species, and (b) line ratio of two different CO isotopologue species at the same rotational-J transition.

Case (a) line ratios probe excitation conditions since the individual line transitions each trace the column density (adjusted by the respective optical depth) for their respective excited level population (e.g., C. D. Wilson et al. 1997; D. Narayanan & M. R. Krumholz 2014; C. H. Peñaloza et al. 2017). In the case of type (b) ratios, the particular reason for variation within and across galaxies can be manifold. It also depends on whether the individual lines that form the ratios are optically thick or thin. The change in ratios can thus be linked to (i) differences in the excitation conditions for only one of the CO isotopologue species, (ii) changes in the abundance of the ^{13}CO and C^{18}O species relative to ^{12}CO, and (iii) changes in the optical depth. A more detailed description on the particular causes and drivers for CO isotopologue line ratio variation is given in T. A. Davis (2014). In the following Sections, we aim to investigate the potential drivers for case (b) each separately and assess their impact based on our observed line ratio trends (Section 3.1) and the insights gained from the CO isotopologue line modeling assuming LTE conditions (Section 3.2) and with RADEX (Section 3.3).

4.1.1. Differences in the Excitation of the Lines

At kiloparsec scales, dB22 ruled out differences in the ^{12}CO and ^{13}CO excitation for M51 based on the fact that the $R_{10}^{13/12}$ and $R_{21}^{13/12}$ showed the same trend across the galaxy. Similarly, we observe that both $R_{10}^{13/12}$ and $R_{21}^{13/12}$ show a decreasing trend with galactocentric radius and an increasing trend with SFR surface density (see Figure 3). Therefore, we conclude that differences in the excitation conditions between the different CO isotopologue species do not have a noticeable effect on the global line ratio trends we see in M51.

4.1.2. Differences in the Relative Abundances

We see evidence for changes in the relative abundances most clearly when looking at the line ratio of two optically thin lines, such as the transitions of ^{13}CO and C^{18}O. Since both line transitions generally remain optically thin, we can link their brightness, to first order, to the subsequent column density. The line ratio therefore gives us a direct measure of the relative abundances of the CO isotopologue species. In the ISM, we differentiate between three major potential drivers of CO isotopologue abundance variations. Here we present a short overview of the potential drivers of isotope abundance variation in question:

1. Selective photodissociation. The less-abundant ^{13}CO and C^{18}O species will be preferentially photodissociated in the presence of stellar populations with O and B stars (E. F. van Dishoeck & J. H. Black 1988). The reason for this is a lower self-shielding (due to lower abundances). Also, differences in the molecular structure cause

different photodissociation rates, though this effect is mainly negligible for ^{13}CO and only marginal for C^{18}O with rates that differ from ^{12}CO by 0.1% and 8%, respectively (R. Visser et al. 2009). Therefore, if selective photodissociation is the main driver for CO isotopologue ratio variation, we expect a strong link with star formation surface density, as OB stars are only short-lived.

2. Chemical fractionation. If the conditions are met, the ^{13}CO abundance will increase due to the exchange reaction (J. Keene et al. 1998)

$$^{12}\mathrm{CO} + ^{13}\mathrm{C}^{+} \rightarrow ^{13}\mathrm{CO} + ^{12}\mathrm{C}^{+}. \quad (9)$$

This reaction is exothermic. As the inverse reaction is endothermic, it will be suppressed under cold ISM conditions (< 10 K). As a result, the ^{13}CO abundance will increase relative to ^{12}CO. Since ^{13}CO emission is optically thin, the increase in its relative abundance to ^{12}CO will affect the subsequent line ratios. We note, however, that in order for this effect to be important, most of the ^{13}CO emission must be coming from gas that still contains significant C^{+}. So in the limit where CO dominates, fractionation will be limited, and changes in the ^{13}CO/^{12}CO ratio abundance vanish. From theoretical considerations in turbulent clouds, L. Szűcs et al. (2014) found that in turbulent clouds, the effect is most significant in lower column densities around $N(^{12}\mathrm{CO}) \sim 10^{16}\,\mathrm{cm}^{-2}$, and becomes negligible at higher column densities beyond $N(^{12}\mathrm{CO}) > 10^{18}\,\mathrm{cm}^{-2}$ (with the corresponding values for ^{13}CO being $N(^{13}\mathrm{CO}) \sim 10^{14}$–$10^{16}\,\mathrm{cm}^{-2}$).

3. Selective nucleosynthesis. The relative CO isotopologue abundances are tracing the star formation history, as different stellar populations lead to different C, N, and O isotope enrichment of the ISM. For instance, massive stars and their supernovae at the end of their stellar lives enrich the ISM mainly with ^{12}C and ^{18}O. The ^{13}C isotope, in contrast, is a byproduct of the Bethe-Weizsäcker cycle (H. A. Bethe 1939). Intermediate-mass stars on the asymptotic giant branch inject the ^{13}C isotope into the ISM via stellar winds (L. J. Sage et al. 1991). Therefore, in the case of nucleosynthesis as main driver, differences in the underlying stellar populations (massive or low-mass stars) will lead to different CO isotopologue line ratios, with larger ^{13}CO abundances (relative to ^{12}CO and C^{18}O) where intermediate-mass stars could inject ^{13}C, while ^{12}CO and C^{18}O abundances increase in the presence of younger stellar populations (i.e., at higher SFR surface densities).

Qualitatively, we can assess the relevance of the aforementioned abundance variation as the main driver based on the sense of the observed line ratio trends with radius or SFR surface density. The $R_{10}^{13/12}$ line ratio shows an increasing trend with star formation surface density (see bottom-center panel in Figure 4). This suggests that selective photodissociation is unlikely the dominant driver of abundance variation since we would expect an opposite trend, as more ^{13}CO is photodissociated in the presence of O and B stars (as traced by higher SFR surface densities). In contrast, the trend agrees with both selective nucleosynthesis and chemical fractionation as key drivers in case of abundance variation. Selective nucleosynthesis could lead, under the assumption of inside-out star formation history, to the observed trend as we expect regions with active star formation to have had more time to build stars and replenish the ISM with ^{13}C ions from intermediate-mass stars. For chemical fractionation, using our median $N(^{13}\mathrm{CO})$ from the LTE analysis ($\log_{10} N(^{13}\mathrm{CO}) = 15.6$), the models from L. Szűcs et al. (2014) predict chemical fractionalization only to be a 20%–30% effect. Also, the increasing $R_{10}^{13/12}$ trend with the SFR surface density (top-center panel in Figure 4) suggests that chemical fractionation is not the main driver, as we would expect the opposite trend as ^{13}CO abundance increases at lower temperatures (i.e., lower SFR surface densities). We note that the slight upturn observed at the lowest SFR surface densities in the plot is more likely related to signal-to-noise effects.

The non-LTE modeling results allow us to be more quantitative about the observed abundance variations: We find overall very low [^{12}CO/^{13}CO] abundance ratio values of ∼40 across the galaxy and only marginally lower values of ∼38 toward the center or disk. These values match observational [^{12}CO/^{13}CO] abundances, which range from 30–60 (see Figure 14 in L. Szűcs et al. 2014, which compiles observational measurements from H. S. Liszt & R. Lucas 1998). Also, earlier studies of M51 have already noted abundance ratios similar to ours. For instance, E. Schinnerer et al. (2010) assumed an abundance ratio of 30 when studying the molecular gas in certain pointings along the southern spiral arm of M51. Furthermore, the low variation that we find in the abundance ratio is a strong indicator that abundance variation is not a main driver for changes in the $R_{10}^{13/12}$ line ratio.

4.1.3. Changes in the Optical Depth

Our RADEX single-zone modeling shows a variation in the ^{12}CO optical depth. This variation is correlated to the $R_{10}^{13/12}$ line ratio (see Figure 10). Indeed, we expect changes in the optical depth, particularly of ^{12}CO, as it will vary proportionally with the gas surface density of the cloud and inverse proportionally with the kinetic temperature of the cloud and the gas velocity dispersion (T. A. D. Paglione et al. 2001). Again, first assessing the line ratio trends qualitatively, we can see that the $R_{10}^{13/12}$ line ratio trend with SFR surface density (top-middle panel in Figure 4) agrees with expected changes in optical depth, as higher SFR surface densities correspond to higher kinetic temperatures and larger velocity dispersion (due to stellar heating of the gas). Such a relation between the SFR surface density and optical depth has been reported by previous studies as well (D. Narayanan & M. R. Krumholz 2014). Moreover, the sharply decreased $R^{13/12}$ ratio toward the center (see Figure 3) is consistent with lower $\tau_{^{12}\mathrm{CO}}$ in centers, and the negative correlation with FWHM is consistent with the scenario that dynamical effects decrease $\tau_{^{12}\mathrm{CO}}$ and increase the ^{12}CO intensity and thus lowering $R^{13/12}$ (Y.-H. Teng et al. 2024).

4.1.4. A Combination of Different Drivers

The derived CO isotopologue line ratio variation in combination with the non-LTE-derived optical depth and isotopologue abundance ratio imply a combination of drivers for different parts of the galaxy. For instance, our results imply an impact of selective nucleosynthesis toward the center. We note that we would expect to see this also reflected in the non-LTE-derived abundance ratio [^{12}CO/^{13}CO]. However, our

detections are too limited in the central region to draw any meaningful conclusions.

4.2. The CO-to-H_2 Conversion Factor

In Sections 3.2 and 3.3, we describe two approaches to estimating the CO-to-H_2 conversion factor. In the following, we will mainly focus on the non-LTE-derived $\alpha_{^{12}\mathrm{CO}(1-0)}$ values, and assess the implications of the observed trends.

As is evident from Figure 11, we detect a flat radial CO-to-H_2 conversion factor trend at $r_{\mathrm{gal}} > 0.5$ kpc and a decrease toward the center. However, due to the faintness of the CO isotopologues at the center, we do not have any non-LTE-derived values at $r \lesssim 0.25$ kpc that could solidify this apparent decrease toward the center, as the CO isotopologue emission becomes too faint. Decreasing $\alpha_{^{12}\mathrm{CO}(1-0)}$ values toward the center are observed in other galaxies (J. S. den Brok et al. 2023b; Y.-H. Teng et al. 2023) and generally associated with lower ^{12}CO emission opacities that increase the emissivity. Indeed, we see evidence of this in Figure 12, as there is a decreasing correlation of $\alpha_{^{12}\mathrm{CO}(1-0)}$ and the line velocity dispersion. We note also that the LTE-derived conversion factor shows a decrease at $r < 0.5$ kpc (Figure 6). In contrast, however, the LTE-derived values also show a mild decrease toward larger radii, which is not observed for the non-LTE-derived radial trend. Overall, both approaches of determining the CO-to-H_2 conversion factor support the conclusion of a more uniform $\alpha_{^{12}\mathrm{CO}}$ value across the disk.

We note that, on average across our map, the LTE yields α_{CO} values significantly lower ($\alpha_{\mathrm{CO}}^{\mathrm{LTE}} \sim 1.0$) and non-LTE techniques values mildly below ($\alpha_{\mathrm{CO}}^{\mathrm{nonLTE}} \sim 2.5$) those reported for similar star-forming galaxies based on dust observations. For instance, the disk-value reported for nearby galaxies by K. M. Sandstrom et al. (2013) is 3.1 $M_{\odot}\,\mathrm{pc}^{-2}/(\mathrm{K\,km\,s}^{-1})$, which is 0.1 dex higher than our galaxy-wide average for the non-LTE-derived value. Our LTE-derived average lies even $\sim$ 0.5 dex below the nearby galaxy average. Furthermore, J. S. den Brok et al. (2023b) reported a even higher dust-based $\alpha_{^{12}\mathrm{CO}}(1-0)$ galaxy-wide average of $4.4 \pm 0.9\,M_{\odot}\,\mathrm{pc}^{-2}/(\mathrm{K\,km\,s}^{-1})$. Finally, E. Schinnerer et al. (2010) also reported a conversion factor similar to the Milky Way value based on a large-scale velocity gradient (LVG) modeling analysis using ^{12}CO and ^{13}CO at 4.″5 in selected parts of the western arm of M51.

But we also note that for some of the galaxies in the sample studied by K. M. Sandstrom et al. (2013), comparable conversion factor values to our findings are reported as well (e.g., for NGC 3627, NGC 4569, NGC 4725, and NGC 4736). And moreover, earlier studies found, in fact, CO-to-H_2 conversion factors below the solar neighborhood value. For instance, S. Garcia-Burillo et al. (1993) derived a value of $\alpha_{^{12}\mathrm{CO}(1-0)} = 1.6$ using an LVG modeling analysis based on ^{12}CO and ^{13}CO. When only using ^{13}CO, they reported a conversion factor of $\alpha_{^{12}\mathrm{CO}(1-0)} = 1$, which is consistent with our LTE-derived value.

To test whether our non-LTE conversion factor values are consistent with dust-based α_{CO} measurements, we calculate the implied dust-to-gas ratio (DGR) based on the CO-to-H_2 conversion factor, the atomic mass surface density (from 21 cm H I observations), and the dust mass surface density (from infrared SED-based measurements). Such data exists at coarser, 26″ resolution and have been presented in J. S. den Brok et al. (2023b). We use the following prescription to obtain

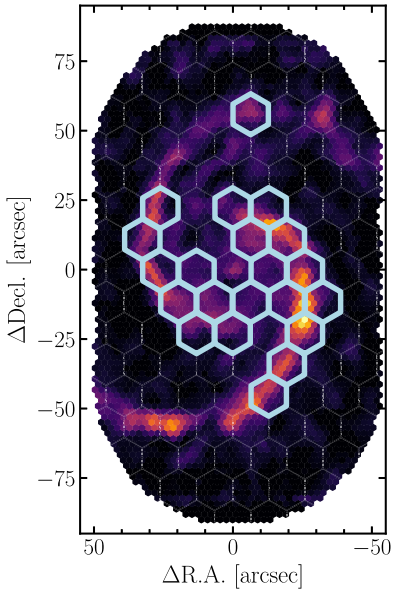

Figure 13. Deriving an estimate for the dust-to-gas ratio (DGR). The background illustrates the ^{12}CO(1–0) moment-0 map at 4″. The larger hexagonal grid indicates the map from J. S. den Brok et al. (2023b) for which we have HI and dust mass measurements (at 26″ resolution). For the blue marked hexagons, we have non-LTE α_{CO} values for >70% in terms of the total ^{12}CO(1–0) intensity from within that pixel.

an estimate of the DGR on kiloparsec scales:

$$\mathrm{DGR} = \frac{\Sigma_{\mathrm{HI}} + \langle \alpha_{\mathrm{CO}} \rangle^{26''} \cdot W_{^{12}\mathrm{CO}(1-0)}^{26''}}{\Sigma_{\mathrm{dust}}}. \quad (10)$$

In Figure 13, we present the 4″ ^{12}CO(1–0) observation of M51. We overplot the coarser 26″ grid on which we have the H I and dust mass surface density observations. Therefore, we have to match our α_{CO} derived at high angular resolution first to the coarser 26″ observations. To do this, we derive a ^{12}CO(1–0) intensity weighted average of the α_{CO} conversion factor per coarse grid point (i.e., $\langle \alpha_{\mathrm{CO}} \rangle^{26''}$ is the luminosity weighted α_{CO}). We can subdivide each 26″ into a set of 4″ grid points for which we have an estimates of α_{CO}. We only compute a weighted average conversion factor (and consequently DGR) for 26″ grid points, which include in their 4″ sub-beams enough $\alpha_{^{12}\mathrm{CO}(1-0)}$ values. For the threshold, the points for which we have a significant $\alpha_{^{12}\mathrm{CO}(1-0)}$ measurement need to contribute >70% of the total ^{12}CO(1–0) intensity from within this hexagonal grid point. Using this approach, we derive an average DGR for the inner $r \lesssim 3$ kpc region of 0.012 ± 0.003, which is within the range of the fiducial value of 0.01 commonly used in the literature.

In general, it is not uncommon to find disagreement between CO-to-H_2 values derived using different techniques. For instance, dust-based CO-to-H_2 estimates do not rely necessarily on a ^{12}CO abundance ratio, but on a dust-to-gas ratio, which also remains uncertain and can explain the 0.2 dex offset to our non-LTE values. In contrast, we also note that the low values we measure within the disk at $r \lesssim 3$ kpc are actually in agreement with values reported for the centers ($r \leqslant 0.5$ kpc) of nearby galaxies (F. P. Israel 2020; Y.-H. Teng et al. 2023).

One major limitation of our non-LTE approach is that we only can use effectively four of the six CO isotopologue lines. The C^{18}O(2–1) emission is too weak and our SMA observations not sensitive enough to detect it across a more extended

region in M51. And only including $C^{18}O(1–0)$ will just allow us to constrain the $C^{18}O$ abundance. However, doing the RADEX modeling fit with only four lines, we need to make assumptions on certain parameters, that ideally, we would want to leave free, such as the volume density width[34] or the beam filling factors. Therefore, to improve the constraints and accuracy of the non-LTE-derived conversion factor, either more sensitive $C^{18}O(2–1)$ observations would be necessary, or higher-J transitions of the ^{12}CO and ^{13}CO could be targeted to fit more free parameters.

4.3. Limitations of Modeling Assumptions

We emphasize that both the LTE and non-LTE line fitting approaches depend on assumptions that can potentially induce bias and lead to inaccurate fitting results. The key assumptions we build into our models are (i) that the conditions can be described by a one-zone model, i.e., homogeneous conditions across a beam, (ii) all of the CO isotopologue emission is originating from the same area/volume, and (iii) the overall CO abundance (in our case, $[^{13}CO/H_2]$) stays constant.

On limitation (i), assuming a one-zone model may oversimplify the complex structure of GMCs, particularly in environments where gradients in density, temperature, or chemical abundances exist on scales smaller than our beam size. Such complexities could result in underestimating or overestimating the derived physical parameters and explain part of the pixel-to-pixel scatter in our results. We emphasize, however, that such a description of the molecular gas using a single component only is widely used in the literature (e.g., F. Ripple et al. 2013; S. Topal et al. 2014; K. Sliwa et al. 2017; D. Cormier et al. 2018; Y.-H. Teng et al. 2022; C. Wang et al. 2023). In particular, when based on low-J ^{12}CO and ^{13}CO line emission, such a modeling approach remains viable for deriving beam-averaged conditions; A. K. Leroy et al. (2017a) found that only for tracers at higher critical density does the beam-averaged emission indeed become sensitive to the particular sub-beam density distribution.

The assumption that all CO isotopologues originate from the same region may also be problematic if selective photodissociation or chemical differentiation causes spatial segregation of different isotopologues. Galactic and extragalactic CO mapping studies indeed appear to show a spatial difference between the origin of ^{12}CO and ^{13}CO emission (e.g., P. F. Goldsmith et al. 2008; J. Pety et al. 2017; J. S. den Brok et al. 2022). However, stacking analyses usually reveal the presence of faint ^{13}CO in all regions bright in ^{12}CO, suggesting that the detection of this isotopologue is generally limited by sensitivity. This supports the use of an identical beam filling factor for the ^{12}CO and ^{13}CO isotopologues and the use of their ratios to trace variation in the overall molecular gas physical conditions. Furthermore, studies in the Orion B cloud complex also reveal a similar behavior of the ^{12}CO, ^{13}CO, and $C^{18}O$ in terms of their variation and trends (e.g., J. Pety et al. 2017; M. Tafalla et al. 2023) with the overall H_2 column density. This suggests that using a single-component approach to derive beam-averaged parameters remains reasonable. Only in the low-density envelope of molecular clouds does the behavior of the different CO isotopologue lines become more uncertain. However, here, the intensities of the emission also drop, therefore limiting the impact on the beam-averaged line ratios.

Finally, we again emphasize that, in particular, the derived α_{CO} value depends critically inversely on the assumed ^{13}CO-to-H_2 abundance ratio. We already discussed the selection and effect of this abundance ratio in Section 3.2.4 and explained why the assumption of a constant abundance ratio is reasonable, at least for a limited region within M51. However, in essence, this means that our derived conversion factor values should be interpreted as α_{CO} per abundance ratio. When comparing the conversion factor with results from other studies, the difference in assumed abundance ratio needs to be accounted for.

Therefore, while we emphasize that our modeling approach is subject to inherent limitations due to the set of assumptions (as are other studies in this field), we argue that they do not significantly compromise the robustness of our results. Nevertheless, these assumptions should be kept in mind when interpreting findings, and future work that resolves finer-scale structures or explores variable abundance ratios will be crucial in refining these models.

4.4. LTE versus Non-LTE Line Fitting

In this study, we examined the emission of CO isotopologue lines using two approaches: LTE and non-LTE. However, both methods depend on certain underlying assumptions. In the ISM, assuming thermalization (i.e., "LTE") is usually not accurate. Instead, to obtain a more precise description of the partition function, it is necessary to solve the equations of statistical equilibrium (i.e., non-LTE calculation). However, this requires detecting several fainter emission lines to determine the different degrees of freedom. In our study, we used four CO isotopologue lines to determine four chemical and physical parameters of the ISM, including temperature, density, column density, and relative isotopologue abundances.

In Figure 14, we provide a direct comparison of the derived quantities from both the LTE and non-LTE approach with other key galactic observables. Strong correlations, which have a Kendall's τ correlation coefficient of $\tau_{Kendall} > 0.5$, are indicated by hatched marker symbols.

Overall, we only find a few strong correlations ($\tau_{Kendall} > 0.5$) for the LTE-derived parameters. The ^{13}CO column density scales significantly with both the $^{13}CO(1–0)$ and $^{12}CO(1–0)$ intensities. The correlation with $^{13}CO(1–0)$ is expected, as it follows from Equation (4). The correlation with $^{12}CO(1–0)$ follows, as we do not find any strong variation of the $R_{10}^{13/12}$ (apart from a depression toward the very center). Finally, we also find a strong positive correlation of the R_{21}^{12} with the excitation temperature, which is expected as the excitation temperature is directly proportional to the peak temperature ratio of ^{12}CO. Previous studies have concluded that with LVG models, it is difficult to constrain any physical parameter within 0.5 dex, with likely even larger uncertainties when accounting for flux calibration uncertainties of 10% (R. Tunnard & T. R. Greve 2016). This could explain the large scatter for our LTE-derived parameters and why there are no significant correlations with key galactic observables.

The non-LTE-derived parameters also show only few strong correlations. We find a strong correlation between the $^{13}CO(1–0)$ intensity and the ^{12}CO column density, indicating that $^{13}CO(1–0)$ is (under some caveats) a good tracer of the amount of molecular gas. As ^{13}CO does generally not become

[34] The volume density width describes the range in volume densities within our beam.

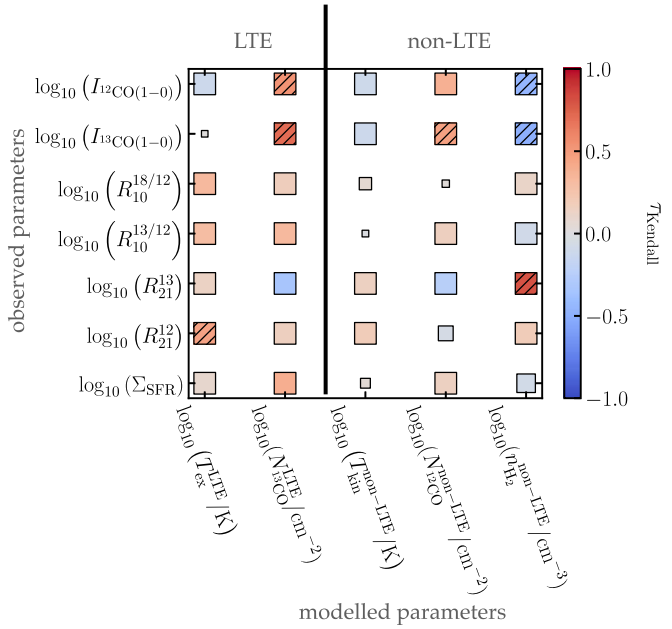

Figure 14. Correlation of LTE and non-LTE parameters. Each box represents the strength of the LTE or non-LTE-derived parameters (on the x-axis) with some key observables or galactic parameters (on the y-axis). We note that we have scaled the non-LTE ^{12}CO column density by the beam filling factor. Red indicates a positive correlation, and blue indicates a negative correlation. The correlation is quantified by the Kendall's τ correlation coefficient. The size of the points indicates the inverse p value (larger points show a significant correlation with $p < 0.05$). Strong correlations, where $|\tau| > 0.5$, are indicated by hatched markers.

optically thick, in contrast to ^{12}CO (see Figure 9), it traces more directly the column density of gas, while the ^{12}CO intensity is more susceptible to changes in opacity. We also find significant negative correlations between the ^{12}CO(1–0) and ^{13}CO(1–0) intensities and the H_2 volume density. The negative correlation could indicate opacity effects, as at large densities, CO becomes more opaque (which follows from the definition of the optical depth, which is the integral along the line of sight of the absorption coefficient, which in turn scales with the volume density). The strong positive correlation of the volume density with the R_{21}^{13} ratio, in contrast, reflects the impact of increasing density on the underlying excitation conditions.

In summary, with the set of four CO isotopologue emission lines at our disposal, the non-LTE-derived parameters do provide improved constraints only in the sense of a decreased scatter. In particular, the ^{13}CO column density and opacity, as well as the CO-to-H_2 conversion factor, agree within the range of scatter with both approaches, at least within the disk. In the center, where conditions become much different from the rest of the galaxy in terms of temperature, density, and dynamics, more emission lines are needed to accurately constrain key parameters such as temperature and density variation at sub-beam scales.

5. Conclusion

We present a multi-CO isotopologue line analysis of M51 combining observations from multiple millimeter-interferometer large programs. This includes ^{12}CO(1–0) data from PAWS, ^{13}CO(1–0), and C^{18}O(1–0) from SWAN, and ^{12}CO(2–1), ^{13}CO(2–1), and C^{18}O(2–1) from the SMA M51 LP survey. All data have angular resolutions of $\leqslant 4''$, which corresponds to a spatial scale of $\leqslant 170$ pc. In combination, we assess the CO isotopologue line ratios across the central $r < 3$ kpc region of M51 and perform LTE and non-LTE line modeling to assess variation in the molecular gas conditions across the different environments of M51. In particular, we find the following.

1. The R_{21}^{12}, R_{21}^{13}, $R_{10}^{13/12}$, $R_{21}^{13/12}$, and $R_{10}^{18/13}$ line ratios all show a mild decreasing radial trend for $r > 0.5$ kpc. In contrast, at $r < 0.5$ kpc, the trends differ. While R_{21}^{12}, R_{21}^{13} significantly increase toward the center, $R_{10}^{13/12}$, $R_{21}^{13/12}$, and $R_{10}^{18/13}$ show all a decrease.
2. We also find an increasing trend of the CO isotopologue line ratios with SFR surface density. In contrast, no line ratio correlates with the ^{12}CO line width, which traces the molecular gas velocity dispersion.
3. Under LTE assumptions, we use the ^{12}CO emission to estimate the excitation temperature and ^{13}CO(1–0) to estimate the ^{13}CO optical depth and column density. Using a fiducial ^{13}CO-to-H_2 abundance ratio of 1.7×10^{-6}, we derive a galaxy-wide CO-to-H_2 conversion factor value at $r \lesssim 3$ kpc of $\sim 0.8\, M_\odot\, \mathrm{pc}^{-2}/(\mathrm{K\,km\,s^{-1}})$. This is a factor 5 below the fiducial value assumed for the MW local neighborhood of 4.3.
4. We use a RADEX grid to model T_{kin}, $n_{\mathrm{H_2}}$, $N_{^{12}\mathrm{CO}}/\Delta v$, and [^{12}CO/^{13}CO]. Using a χ^2 minimization approach, we fit these parameters to the observed line intensities to find the best-fit molecular gas conditions. We convert the derived ^{12}CO column densities into an estimate of the CO-to-H_2 conversion factor. We find a nearly flat trend of $\alpha_{^{12}\mathrm{CO}(1-0)}^{\mathrm{non-LTE}} \approx 2.4\, M_\odot\, \mathrm{pc}^{-2}/(\mathrm{K\,km\,s^{-1}})$, which is 0.3 dex larger than the LTE value.

Contrasting LTE and non-LTE-derived parameters, we note that the non-LTE approach produces lower scatter. The LTE approach also seems to underestimate the column density by a factor 2–3. For a more robust non-LTE approach, more high-J CO isotopologue lines are required to obtain constraints also on the sub-beam density distribution and/or beam filling factor. Given the simplistic one-zone model, we emphasize that the LTE and non-LTE-derived values must be interpreted carefully when contrasting with Galactic or other extragalactic work using different modeling prescriptions.

Overall, these results highlight the diverse nature of the molecular ISM in nearby galaxies with clear differences between the various galactic environments. The results highlight that when assessing the molecular gas properties using CO observations, we need to account for the particular galactic environment.

Acknowledgments

This work was carried out as part of the PHANGS collaboration. We thank the anonymous reviewer for their careful reading of the manuscript and their insightful feedback and suggestions. This work is based on observations carried out under project ID M19AA with the IRAM NOEMA Interferometer. IRAM is supported by INSU/CNRS (France), MPG (Germany), and IGN (Spain). We also use data from the Submillimeter Array which is a joint project between the Smithsonian Astrophysical Observatory and the Academia Sinica Institute of Astronomy and Astrophysics and is funded by the Smithsonian Institution and the Academia Sinica. We

recognize that Maunakea is a culturally important site for the indigenous Hawaiian people; we are privileged to study the cosmos from its summit. J.d.B. and E.K. acknowledge support from the Smithsonian Institution as Submillimeter Array (SMA) Fellows. M.J.J.D., A.U., and M.Q. acknowledge support from the Spanish grant PID2022-138560NB-I00, funded by MCIN/AEI/10.13039/501100011033/FEDER, EU. E.S. acknowledges funding from the European Research Council (ERC) under the European Union's Horizon 2020 research and innovation program (grant agreement No. 694343). K.S. and Y.-H. T. acknowledge funding support from the National Science Foundation (NSF) under grant No. 2108081. E.R. and Engineering Research Council of Canada (NSERC), funding reference number RGPIN-2022-03499. P.K. H. gratefully acknowledges the Fundação de Amparo à Pesquisa do Estado de São Paulo (FAPESP) for the support grant 2023/14272-4. S.K.S. acknowledges financial support from the German Research Foundation (DFG) via Sino-German research grant SCHI 536/11-1. M.C. gratefully acknowledges funding from the Deutsche Forschungsgemeinschaft (DFG; German Research Foundation) through an Emmy Noether Research Group (grant No. CH2137/1-1). COOL Research DAO is a Decentralised Autonomous Organisation supporting research in astrophysics aimed at uncovering our cosmic origins. H.A.P. acknowledges support from the National Science and Technology Council of Taiwan under grant 110-2112-M-032-020-MY3.

Facility: Smithsonian Astrophysical Observatory (SAO)/Academia Sinica SubMillimeter Array (SMA) at Mauna Kea Observatory, Institut de radioastronomie millimétrique (IRAM) telescopes, Extended Very Large Array (EVLA).

Software: astropy (Astropy Collaboration et al. 2013, 2018), SpectralCube (A. Ginsburg et al. 2015), PyStructure (J. den Brok et al. 2024).

Appendix A
SMA Data Reduction

We use observations from the Submillimeter Array M51 Large Program (2016B-S035; PI: K. Sliwa). In the following, we briefly describe the observations, data calibration, imaging, and short-spacing correction that we used to produce the data cubes.

A.1. SMA Observations and Data Calibration

The SMA observed M51 using three different configurations split into 14 different tracks over the course of 2017. We note that if the sensitivity requirements of the individual tracks were not achieved, we obtained additional, further tracks. Table 6 provides an overview of all of the observations of this program. The main tracks 1–6 are done with the SMA in compact (COM) configuration. These consist of 55 pointings such that the resulting FOV matches the one from PAWS (see Figure 1). Track 8 consists of SMA extended (EXT) configuration observations. The remaining tracks 9–14 are done using the SMA subcompact (SUB) configuration. For the SUB configuration observations, the observations consist of more pointings, resulting in a larger FOV (see the SMA outline shown in Figure 1). Apart from track 7, all tracks could be observed under sufficient weather conditions with nightly average $\langle \mathrm{pwv} \rangle \lesssim 4$ mm.

Table 6
Summary of Observations

Track		Date [mm/dd/yy]	Configuration	⟨pwv⟩ (mm)	On-source Time (hr)
1	a	04/17/2017	COM	0.8	3.4
2	a	04/19/2017	COM	2.1	5.6
	b	05/04/2017	COM	1.5	5.2
3	a	04/29/2017	COM	1.8	5.3
4	a	04/15/2017	COM	1.1	5.5
5	a	04/14/2017	COM	4.1	3.3
	b	04/26/2017	COM	4.3	4.9
6	a	04/13/2017	COM	2.6	3.2
7	a	05/03/2017	COM	7.1	⋯
	a	02/22/2017	EXT	2.0	8.4
8	b	02/27/2017	EXT	3.3	2.9
	c	03/07/2017	EXT	3.1	4.6
9	a	01/24/2017	SUB	1.6	3.2
10	a	02/09/2017	SUB	1.3	3.4
11	a	05/28/2017	SUB	2.1	3.0
12	a	02/13/2017	SUB	2.6	2.4
	b	02/15/2017	SUB	1.6	3.4
	a	05/22/2017	SUB	3.3	3.2
13	b	05/27/2017	SUB	1.1	3.0
	c	06/01/2017	SUB	2.8	3.1
14	a	02/10/2017	SUB	2.3	3.5

The SMA data calibration was performed using the MIR software package.[35] Flux calibrators were, depending on availability during the night, either Titan, Jupiter, or Saturn. For the bandpass, the SMA observed either 3c84 or 3c454.3. As gain calibrator, two sources were observed throughout the night (two of the following: 1419+543, 1310+323, and 1153+495).

A.2. Imaging

We first convert calibrated visibilities into a measurement set readable in `CASA` (J. P. McMullin et al. 2007). This step is needed so that we can use the PHANGS-ALMA imaging pipeline (A. K. Leroy et al. 2021).[36] We add scan intents to the SMA data to mimic the ALMA format. The pipeline first transforms the visibility data to a user-given channel width and frequency range, that corresponds to the line plus line-free channels. Unlike for ALMA data, we avoid reweighting the data as the SMA's data weights are calibrated to system temperature, accurately reflecting the measurement uncertainty. Next, the continuum emission is subtracted. Then a two-stage cleaning process is started using the task `CASA tclean`. The task `tclean` was run iteratively to force numerous large cycles (improving the accuracy of the deconvolution). The first stage consists of a multiscale cleaning down to $\sim 4\sigma$. For the second stage, a single-scale cleaning is performed down to $\sim 1\sigma$. In addition, as part of the second stage, a clean mask is computed at each iteration. This clean mask is constructed using a watershed algorithm that extracts all $>2\sigma$ pixels connected to $>4\sigma$ peaks.

Since the SUB and COM observations have a different number of pointings, and CASA cannot deal with significant spatial variations in the PSF within a single mosaic, we

[35] https://lweb.cfa.harvard.edu/~cqi/mircook.html
[36] https://github.com/akleroy/phangs_imaging_scripts/

removed pointings in the SUB field that did not have a matching pointing in the COM observations. Furthermore, the $C^{18}O(2–1)$ line falls within the edge of chunks (spectral windows) 1 and 2 of the lower sideband, so we stitched together the two sidebands using the `CASA concat` and `mstransform` functions.

A.3. Short-spacing Correction and Post-processing

We use the PHANGS-ALMA post-processing pipeline, which is an extension of the PHANGS-ALMA imaging pipeline for the short-spacing correction. The post-processing routine first uses the `CASA feather` routine for the short-spacing correction. We use the IRAM 30 m data from CLAWS (dB22) for the single-dish data. Then the pipeline corrects the resulting images for the primary beam attenuation and converts them to Kelvin units.

In Figure 15, we present a rudimentary analysis of the short-spacing corrected data. The top two panels show the averaged spectra over the entire FOV. For $^{12}CO(2–1)$, we find that 50% of the flux appears to be missing in the interferometric data. This degree of diffuse emission is similar to what J. Pety et al. (2013) reported for the $^{12}CO(1–0)$. To verify that this discrepancy is not the result of flux calibration uncertainties, we match the amplitudes of the visibilities in the overlapping *uv* space of the SMA and IRAM 30 m data using the `uvcombine` package (E. Koch & A. Ginsburg 2022). The *uv* overlap extends from $\sim 12''$ (resolution of IRAM 30 m data) to $\sim 28''$ (largest recoverable scales of the SMA in SUB configuration). As is evident from the distribution of the visibilities in the overlapping *uv* space, the visibilities agree within the noise variation (ratio of 1.09 ± 0.07 for interferometric versus single-dish flux), indicating consistent flux calibrations for the two data sets.

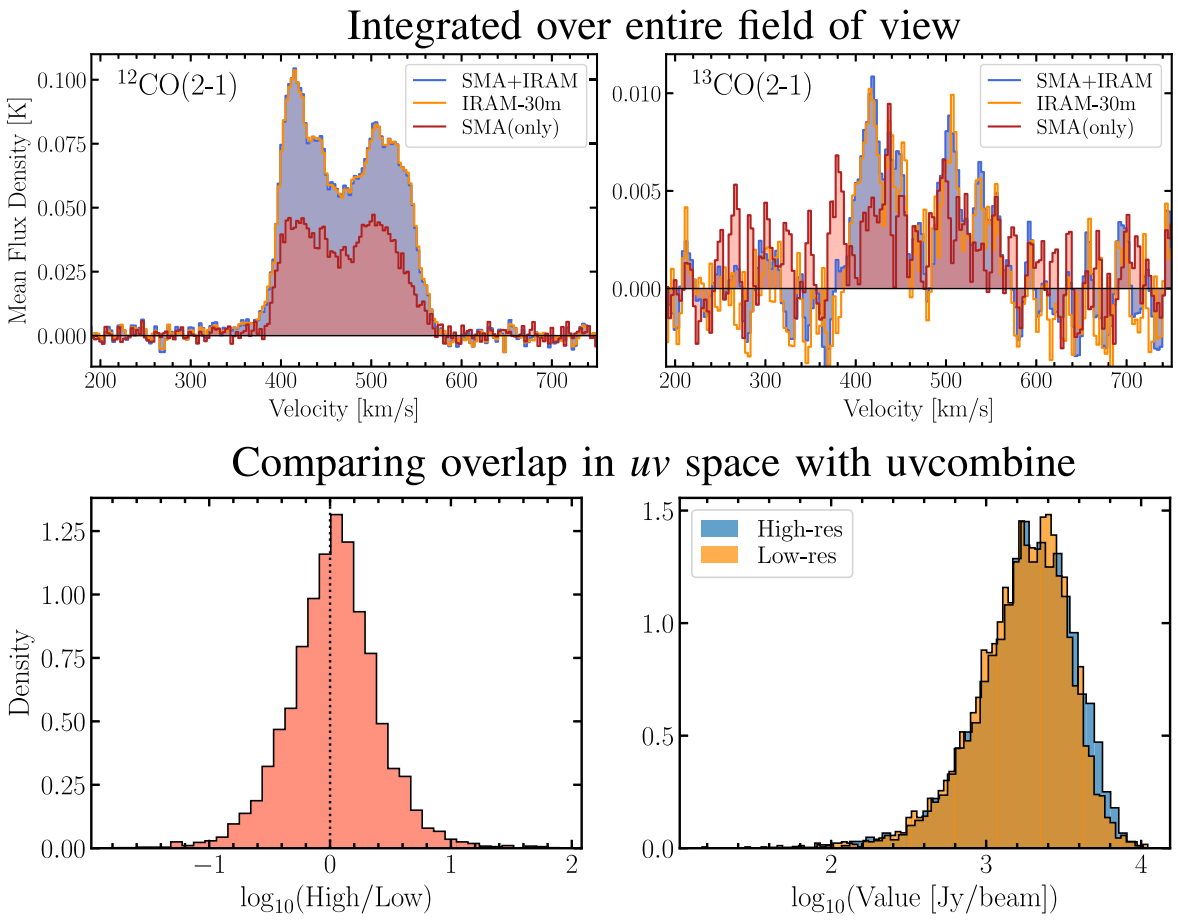

Figure 15. Short-spacing correction analysis. The top panels show the $^{12}CO(2–1)$ (top-left panel) and $^{13}CO(2–1)$ (top-right panel) spectra, averaged over the entire FOV. We obtain the red spectrum when using only the SMA SUB+COM cube. After short-spacing correction (SMA+IRAM), we obtain the blue spectrum. For ^{12}CO (2–1), it is evident that half of the emission is missing in the interferometric data. The lower panels show the amplitudes in the overlapping *uv* space of the IRAM and SMA data (ranging from $13''$–$28''$) ratio of the amplitudes (bottom-left panel), and the amplitude distribution (bottom-right panel) for the high- (SMA) and low- (IRAM 30 m) resolution data separately.

Appendix B
Extent of Significant Line Ratio Detections

For the line ratio analysis, we focus primarily on sight lines for which both lines forming the ratio are significantly (i.e., $S/N > 5$) detected. Since the sensitivity of the different observations and the strength of the different lines varies, the number of significant detections changes. In Figure 16, we illustrate the spatial distribution for the significantly detected sight lines per line ratio for the ratios presented in Figures 3 and 4.

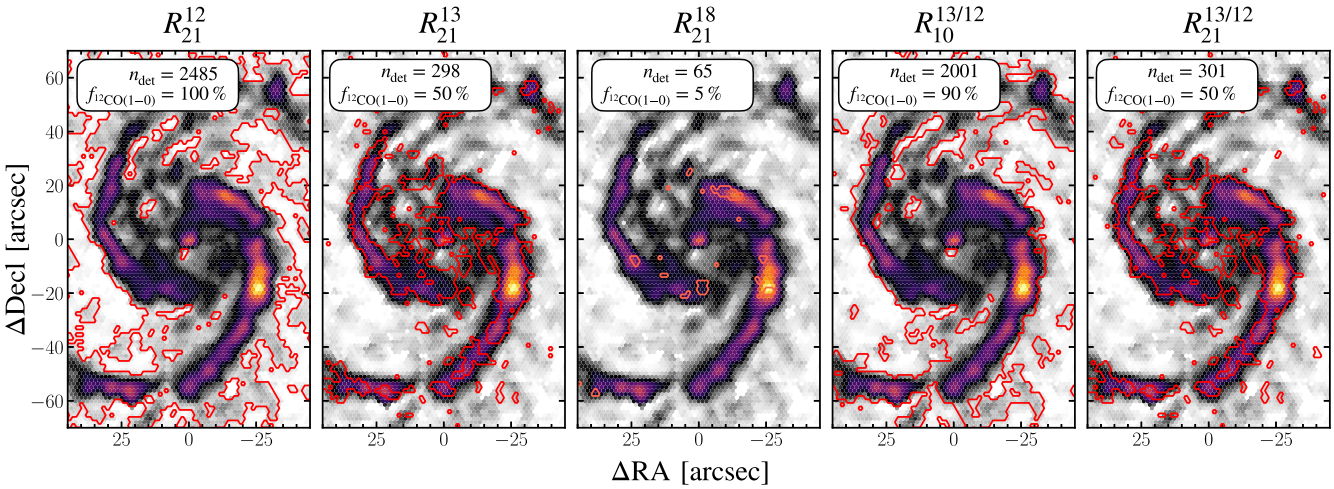

Figure 16. Significant (5σ) line ratio detection. Each panels illustrates the sight lines per line ratio for which both lines are significantly detected at $S/N > 5$ by the red contour. For reference, each panel also lists the number of sight lines and the percentage of ^{12}CO(1–0) flux contained for the selected sight lines in the top-left corner. The sight lines are colored by the CO(1–0) moment-0 to show M51's morphology.

Appendix C
RADEX Non-LTE Grid

For our non-LTE line modeling approach, we construct a parameter grid using RADEX (F. F. S. van der Tak et al. 2007). This grid contains the simulated integrated intensities of the CO isotopologues for the various permutations of free parameters. The free parameters are the kinetic temperature, $T_{\rm kin}$, the H_2 volume density, $n_{\rm H_2}$, the CO column density per line width, $N_{\rm CO}/\Delta v$, and the CO isotopologue abundance ratio [^{12}CO/^{13}CO]. The range of parameter values used to generate the grid are described in Table 3. We fix the ^{12}CO line width, Δv, to 15 km s^{-1}. We provide the entire Table of simulated intensity in machine-readable format in Table 7.

Table 7
RADEX Single-zone Modeled Line Intensities

$T_{\rm kin}$ (K)	$n_{0,\,\rm H_2}$ (cm^{-3})	$N_{\rm CO}/\Delta v$ (cm^{-2}/km/s^{-1})	[^{12}CO/^{13}CO]	ϕ	$\tau_{^{12}\rm CO}$	$\tau_{^{13}\rm CO}$	$W(^{12}\rm CO(1-0))$ (K km s^{-1})	⋯
4.0	100.0	5×10^{14}	20	0.01	0.571	0.0274	0.0035	
4.0	100.0	7.925×10^{14}	20	0.01	0.9014	0.0435	0.0057	
4.0	100.0	1.256×10^{15}	20	0.01	1.419	0.0689	0.0090	
4.0	100.0	1.991×10^{15}	20	0.01	2.2240	0.1091	0.0142	
4.0	100.0	3.155×10^{15}	20	0.01	3.463	0.1728	0.0218	
⋮	⋮	⋮	⋮	⋮	⋮	⋮	⋮	⋮
100	10^5	1.991×10^{18}	80	1	5.640	0.0649	1528	
100	10^5	3.155×10^{18}	80	1	8.904	0.1021	1534	
100	10^5	5.0×10^{18}	80	1	14.07	0.1612	1535	

(This table is available in its entirety in machine-readable form in the online article.)

ORCID iDs

Jakob den Brok https://orcid.org/0000-0002-8760-6157
María J. Jiménez-Donaire https://orcid.org/0000-0002-9165-8080
Adam Leroy https://orcid.org/0000-0002-2545-1700
Eva Schinnerer https://orcid.org/0000-0002-3933-7677
Frank Bigiel https://orcid.org/0000-0003-0166-9745
Jérôme Pety https://orcid.org/0000-0003-3061-6546
Glen Petitpas https://orcid.org/0009-0005-2122-0680
Antonio Usero https://orcid.org/0000-0003-1242-505X
Yu-Hsuan Teng https://orcid.org/0000-0003-4209-1599
Pedro Humire https://orcid.org/0000-0003-3537-4849
Eric W. Koch https://orcid.org/0000-0001-9605-780X
Erik Rosolowsky https://orcid.org/0000-0002-5204-2259
Karin Sandstrom https://orcid.org/0000-0002-4378-8534
Daizhong Liu https://orcid.org/0000-0001-9773-7479
Qizhou Zhang https://orcid.org/0000-0003-2384-6589
Sophia Stuber https://orcid.org/0000-0002-9333-387X
Mélanie Chevance https://orcid.org/0000-0002-5635-5180
Daniel A. Dale https://orcid.org/0000-0002-5782-9093
Cosima Eibensteiner https://orcid.org/0000-0002-1185-2810
Ina Galić https://orcid.org/0009-0002-9819-1468
Simon C. O. Glover https://orcid.org/0000-0001-6708-1317
Hsi-An Pan https://orcid.org/0000-0002-1370-6964
Miguel Querejeta https://orcid.org/0000-0002-0472-1011
Rowan J. Smith https://orcid.org/0000-0002-0820-1814
Thomas G. Williams https://orcid.org/0000-0002-0012-2142
David J. Wilner https://orcid.org/0000-0003-1526-7587
Valencia Zhang https://orcid.org/0009-0007-2660-7635

References

Aladro, R., Viti, S., Bayet, E., et al. 2013, A&A, 549, A39
Astropy Collaboration, Price-Whelan, A. M., Sipőcz, B. M., et al. 2018, AJ, 156, 123
Astropy Collaboration, Robitaille, T. P., Tollerud, E. J., et al. 2013, A&A, 558, A33
Baker, P. L. 1976, A&A, 50, 327
Berg, D. A., Pogge, R. W., Skillman, E. D., et al. 2020, ApJ, 893, 96
Bethe, H. A. 1939, PhRv, 55, 103
Bialy, S., & Sternberg, A. 2015, MNRAS, 450, 4424
Bigiel, F., Leroy, A., Walter, F., et al. 2008, AJ, 136, 2846
Bolatto, A. D., Wolfire, M., & Leroy, A. K. 2013, ARA&A, 51, 207
Braine, J., Gratier, P., Kramer, C., et al. 2010, A&A, 520, A107
Brown, T., & Wilson, C. D. 2019, ApJ, 879, 17
Brown, T., Wilson, C. D., Zabel, N., et al. 2021, ApJS, 257, 21
Caldú-Primo, A., Schruba, A., Walter, F., et al. 2013, AJ, 146, 150
Cao, Y., Wong, T., Bolatto, A. D., et al. 2023, ApJS, 268, 3
Cormier, D., Bigiel, F., Jiménez-Donaire, M. J., et al. 2018, MNRAS, 475, 3909
Costagliola, F., Aalto, S., Rodriguez, M. I., et al. 2011, A&A, 528, A30
Croxall, K. V., Pogge, R. W., Berg, D. A., Skillman, E. D., & Moustakas, J. 2015, ApJ, 808, 42
Dahmen, G., Huttemeister, S., Wilson, T. L., & Mauersberger, R. 1998, A&A, 331, 959
Davis, T. A. 2014, MNRAS, 445, 2378
den Brok, J., Neumann, L., Eibensteiner, C., et al. 2024, PyStructure software, v3.0.1, Zenodo, doi:10.5281/zenodo.13787728
den Brok, J. S., Bigiel, F., Chastenet, J., et al. 2023b, A&A, 676, A93
den Brok, J. S., Bigiel, F., Sliwa, K., et al. 2022, A&A, 662, A89
den Brok, J. S., Leroy, A. K., Usero, A., et al. 2023a, MNRAS, 526, 6347
Dickman, R. L. 1978, ApJS, 37, 407
Frerking, M. A., Langer, W. D., & Wilson, R. W. 1982, ApJ, 262, 590
Garcia-Burillo, S., Guelin, M., & Cernicharo, J. 1993, A&A, 274, 123
Ginsburg, A., Robitaille, T., Beaumont, C., & ZuHone, J. 2015, Release Candidate 2—includes yt interop, v0.2-rc2, Zenodo, doi:10.5281/zenodo.11485
Goldsmith, P. F., Heyer, M., Narayanan, G., et al. 2008, ApJ, 680, 428
He, H., Wilson, C. D., Sun, J., et al. 2024, ApJ, 971, 176
Henkel, C., Asiri, H., Ao, Y., et al. 2014, A&A, 565, A3
Heyer, M. H., & Brunt, C. M. 2004, ApJL, 615, L45
Israel, F. P. 2020, A&A, 635, A131
Ivezić, Ž., Connolly, A. J., VanderPlas, J. T., & Gray, A. 2014, Statistics, Data Mining, and Machine Learning in Astronomy: a Practical Python Guide for the Analysis of Survey Data (Princeton, NJ: Princeton Univ. Press)
Jiménez-Donaire, M. J., Bigiel, F., Leroy, A. K., et al. 2019, ApJ, 880, 127
Jiménez-Donaire, M. J., Cormier, D., Bigiel, F., et al. 2017, ApJL, 836, L29
Kainulainen, J., Beuther, H., Henning, T., & Plume, R. 2009, A&A, 508, L35
Kamenetzky, J., Rangwala, N., Glenn, J., Maloney, P. R., & Conley, A. 2014, ApJ, 795, 174
Keene, J., Schilke, P., Kooi, J., et al. 1998, ApJL, 494, L107
Kennicutt, R. C., & Evans, N. J. 2012, ARA&A, 50, 531
Koch, E., & Ginsburg, A., 2022 uvcombine: Combine Images with Different Resolutions, Astrophysics Source Code Library, ascl:2208.014
Koda, J., Sawada, T., Wright, M. C. H., et al. 2011, ApJS, 193, 19
Koda, J., Scoville, N., Hasegawa, T., et al. 2012, ApJ, 761, 41
Langer, W. D., & Penzias, A. A. 1990, ApJ, 357, 477
Leroy, A. K., Hughes, A., Liu, D., et al. 2021, ApJS, 255, 19
Leroy, A. K., Rosolowsky, E., Usero, A., et al. 2022, ApJ, 927, 149
Leroy, A. K., Schinnerer, E., Hughes, A., et al. 2017b, ApJ, 846, 71
Leroy, A. K., Usero, A., Schruba, A., et al. 2017a, ApJ, 835, 217
Leroy, A. K., Walter, F., Brinks, E., et al. 2008, AJ, 136, 2782
Linden, S. T., Murphy, E. J., Dong, D., et al. 2020, ApJS, 248, 25
Liszt, H. S., & Lucas, R. 1998, A&A, 339, 561
Liu, D., Schinnerer, E., Cao, Y., et al. 2023, ApJL, 944, L19
Martín, S., Muller, S., Henkel, C., et al. 2019, A&A, 624, A125
McMullin, J. P., Waters, B., Schiebel, D., Young, W., & Golap, K. 2007, in ASP Conf. Ser. 376, Astronomical Data Analysis Software and Systems XVI, ed. R. A. Shaw, F. Hill, & D. J. Bell (San Francisco, CA: ASP), 127
McQuinn, K. B. W., Skillman, E. D., Dolphin, A. E., Berg, D., & Kennicutt, R. 2016, ApJ, 826, 21
Meier, D. S., & Turner, J. L. 2004, AAS Meeting Abstracts, 205, 99.09
Milam, S. N., Savage, C., Brewster, M. A., Ziurys, L. M., & Wyckoff, S. 2005, ApJ, 634, 1126
Morokuma-Matsui, K., Sorai, K., Sato, Y., et al. 2020, PASJ, 72, 90
Murphy, E. J., Condon, J. J., Schinnerer, E., et al. 2011, ApJ, 737, 67
Murphy, E. J., Dong, D., Momjian, E., et al. 2018, ApJS, 234, 24
Narayanan, D., & Krumholz, M. R. 2014, MNRAS, 442, 1411
Neumann, L., den Brok, J. S., Bigiel, F., et al. 2023, A&A, 675, A104
Nishimura, A., Tokuda, K., Kimura, K., et al. 2015, ApJS, 216, 18
Padoan, P., & Nordlund, Å. 2002, ApJ, 576, 870
Paglione, T. A. D., Wall, W. F., Young, J. S., et al. 2001, ApJS, 135, 183
Pan, H.-A., Kuno, N., Koda, J., et al. 2015, ApJ, 815, 59
Peñaloza, C. H., Clark, P. C., Glover, S. C. O., Shetty, R., & Klessen, R. S. 2017, MNRAS, 465, 2277
Pety, J., Guzmán, V. V., Orkisz, J. H., et al. 2017, A&A, 599, A98
Pety, J., Schinnerer, E., Leroy, A. K., et al. 2013, ApJ, 779, 43
Pineda, J. E., Caselli, P., & Goodman, A. A. 2008, ApJ, 679, 481
Querejeta, M., Schinnerer, E., Schruba, A., et al. 2019, A&A, 625, A19
Rigopoulou, D., Lawrence, A., White, G. J., Rowan-Robinson, M., & Church, S. E. 1996, A&A, 305, 747
Ripple, F., Heyer, M. H., Gutermuth, R., Snell, R. L., & Brunt, C. M. 2013, MNRAS, 431, 1296
Roueff, A., Gerin, M., Gratier, P., et al. 2021, A&A, 645, A26
Sage, L. J., Mauersberger, R., & Henkel, C. 1991, A&A, 249, 31
Salak, D., Nakai, N., & Kitamoto, S. 2014, PASJ, 66, 96
Sandstrom, K. M., Leroy, A. K., Walter, F., et al. 2013, ApJ, 777, 5
Schinnerer, E., Meidt, S. E., Pety, J., et al. 2013, ApJ, 779, 42
Schinnerer, E., Weiß, A., Aalto, S., & Scoville, N. Z. 2010, ApJ, 719, 1588
Schmidt, M. 1959, ApJ, 129, 243
Schöier, F. L., van der Tak, F. F. S., van Dishoeck, E. F., & Black, J. H. 2005, A&A, 432, 369
Schruba, A., Leroy, A. K., Walter, F., et al. 2011, AJ, 142, 37
Schuster, K. F., Kramer, C., Hitschfeld, M., Garcia-Burillo, S., & Mookerjea, B. 2007, A&A, 461, 143
Sheffer, Y., Rogers, M., Federman, S. R., et al. 2008, ApJ, 687, 1075
Shetty, R., Glover, S. C., Dullemond, C. P., et al. 2011, MNRAS, 415, 3253
Shirley, Y. L. 2015, PASP, 127, 299
Sliwa, K., Wilson, C. D., Matsushita, S., et al. 2017, ApJ, 840, 8
Sliwa, K., Wilson, C. D., Petitpas, G. R., et al. 2012, ApJ, 753, 46

Stuber, S. K., Pety, J., Schinnerer, E., et al. 2023, A&A, 680, L20
Szűcs, L., Glover, S. C. O., & Klessen, R. S. 2014, MNRAS, 445, 4055
Szűcs, L., Glover, S. C. O., & Klessen, R. S. 2016, MNRAS, 460, 82
Tafalla, M., Usero, A., & Hacar, A. 2023, A&A, 679, A112
Teng, Y.-H., Chiang, I.-D., Sandstrom, K. M., et al. 2024, ApJ, 961, 42
Teng, Y.-H., Sandstrom, K. M., Sun, J., et al. 2022, ApJ, 925, 72
Teng, Y.-H., Sandstrom, K. M., Sun, J., et al. 2023, ApJ, 950, 119
Topal, S., Bayet, E., Bureau, M., Davis, T. A., & Walsh, W. 2014, MNRAS, 437, 1434
Tosaki, T., Hasegawa, T., Shioya, Y., Kuno, N., & Matsushita, S. 2002, PASJ, 54, 209
Tunnard, R., & Greve, T. R. 2016, ApJ, 819, 161
van der Tak, F. F. S., Black, J. H., Schöier, F. L., Jansen, D. J., & van Dishoeck, E. F. 2007, A&A, 468, 627
van Dishoeck, E. F., & Black, J. H. 1988, ApJ, 334, 771
van Dishoeck, E. F., Glassgold, A. E., Guelin, M., et al. 1992, in IAU Symp. 150, Astrochemistry of Cosmic Phenomena, ed. P. D. Singh (Cambridge: Cambridge Univ. Press), 285
Visser, R., van Dishoeck, E. F., & Black, J. H. 2009, A&A, 503, 323
Wang, C., Feng, H., Yang, J., et al. 2023, AJ, 166, 121
Wilson, C. D., Walker, C. E., & Thornley, M. D. 1997, ApJ, 483, 210
Wilson, T. L., Rohlfs, K., & Hüttemeister, S. 2009, Tools of Radio Astronomy (Berlin: Springer)
Wilson, T. L., & Rood, R. 1994, ARA&A, 32, 191
Yajima, Y., Sorai, K., Miyamoto, Y., et al. 2021, PASJ, 73, 257
Yan, Y. T., Henkel, C., Kobayashi, C., et al. 2023, A&A, 670, A98
Yang, B., Stancil, P. C., Balakrishnan, N., & Forrey, R. C. 2010, ApJ, 718, 1062
Young, J. S., & Scoville, N. 1982, ApJ, 258, 467